LZTR1 polymerization provokes cardiac pathology in recessive Noonan syndrome

Alexandra Viktoria Busley, MSc[1,2,3], Óscar Gutiérrez-Gutiérrez, PhD[1,2], Elke Hammer, PhD[2,4], Martin Steinegger, PhD[5], Linda Böhmer, BSc[1], Henning Schroeder, PhD[6], Mandy Kleinsorge, PhD[1,2,], Janine Altmüller, MD[7,8], Felix Marbach, MD[9,10], Gerd Hasenfuss, MD[1,2,3], Wolfram-Hubertus Zimmermann, MD[2,3,11], Bernd Wollnik, MD[2,3,12], Lukas Cyganek, PhD[1,2,3,*]

[1]Stem Cell Unit, Clinic for Cardiology and Pneumology, University Medical Center Göttingen, Göttingen, Germany; [2]DZHK (German Center for Cardiovascular Research), partner site Göttingen and Greifswald, Germany; [3]Cluster of Excellence "Multiscale Bioimaging: from Molecular Machines to Networks of Excitable Cells" (MBExC), University of Göttingen, Göttingen, Germany; [4]Interfaculty Institute of Genetics and Functional Genomics, University Medicine Greifswald, Greifswald, Germany; [5]School of Biological Sciences, Seoul National University, Seoul, South Korea; [6]NMR Signal Enhancement Group, Max Planck Institute for Multidisciplinary Sciences , Göttingen, Germany; [7]Cologne Center for Genomics, University of Cologne, Faculty of Medicine and University Hospital Cologne, Cologne, Germany; [8]Genomics Platform, Berlin Institute for Medical Systems Biology, Max-Delbrück-Center for Molecular Medicine Berlin, Berlin, Germany; [9]Institute of Human Genetics, University Hospital Cologne, Cologne, Germany; [10]Institute of Human Genetics, Heidelberg University, Heidelberg, Germany; [11]Institute of Pharmacology and Toxicology, University Medical Center Göttingen, Göttingen, Germany; [12]Institute of Human Genetics, University Medical Center Göttingen, Göttingen, Germany.

*Corresponding author: lukas.cyganek@gwdg.de

Address for correspondence:

Dr. Lukas Cyganek

Clinic for Cardiology and Pneumology

University Medical Center Göttingen

Robert-Koch-Str. 40, 37075 Göttingen, Germany

Tel: +49 551 39 64280, Mail: lukas.cyganek@gwdg.de

Running title:

LZTR1 polymerization causes hypertrophy

Abstract

Noonan syndrome patients harboring causative variants in *LZTR1* are particularly at risk to develop severe and early-onset hypertrophic cardiomyopathy. However, the underling disease mechanisms of *LZTR1* missense variants driving the cardiac pathology are poorly understood. Hence, therapeutic options for Noonan syndrome patients are limited. In this study, we investigated the mechanistic consequences of a novel homozygous causative variant $LZTR1^{L580P}$ by using patient-specific and CRISPR/Cas9-corrected iPSC-cardiomyocytes. Molecular, cellular, and functional phenotyping in combination with *in silico* prediction of protein complexes uncovered a unique $LZTR1^{L580P}$-specific disease mechanism provoking the cardiac hypertrophy. The homozygous variant was predicted to alter the binding affinity of the dimerization domains facilitating the formation of linear LZTR1 polymer chains. The altered polymerization resulted in dysfunction of the LZTR1-cullin 3 ubiquitin ligase complexes and subsequently, in accumulation of RAS GTPases, thereby provoking global pathological changes of the proteomic landscape ultimately leading to cellular hypertrophy. Importantly,

uni- or biallelic genetic correction of the *LZTR1*^{L580P} missense variant rescued the molecular and cellular disease-associated phenotype, providing proof-of-concept for CRISPR-based gene therapies.

Keywords

Cardiomyocytes / Hypertrophic cardiomyopathy / iPSCs / LZTR1 / Noonan syndrome

Introduction

Noonan syndrome (NS) is a multi-systemic developmental disorder with a broad spectrum of symptoms and varying degrees of disease severity. Common clinical symptoms range from intellectual disability, facial dysmorphisms, webbed neck, skeletal deformities, short stature, and in many cases congenital heart disease.[1] With a prevalence of approximately 1 in 1,000 – 2,500 live births, NS is considered the most common monogenic disease associated with congenital heart defects and early-onset hypertrophic cardiomyopathy (HCM).[2] Young NS patients diagnosed with HCM are more prone to develop heart failure accompanied by a poor late survival in contrast to patients suffering from non-syndromic HCM.[3,4] Like other phenotypically overlapping syndromes classified as RASopathies, NS is caused by variants in RAS-mitogen-activated protein kinase (MAPK)-associated genes, all typically leading to an increase in signaling transduction.[5] Within the RASopathy spectrum, patients harboring causative gene variants in *RAF1*, *HRAS*, *RIT1* and *LZTR1* are particularly at risk to develop severe and early-onset HCM.[6,7]

Recent studies from others and our group revealed the functional role of LZTR1 within the RAS-MAPK signaling cascade as a negative regulator of signaling activity. *LZTR1* encodes an adapter protein of the cullin 3 ubiquitin ligase complex by selectively targeting RAS proteins as substrates for degradation. *LZTR1* deficiency – caused by truncating or missense variants – results in an accumulation of the RAS protein pool and, as a consequence, in RAS-MAPK signaling hyperactivity.[8–10] Whereas dominant *LZTR1* variants generally cluster in the Kelch motif perturbing RAS binding to the ubiquitination complex,[11] the mechanistic consequences of recessive *LZTR1* missense variants, which are distributed over the entire protein, are not understood.

Human induced pluripotent stem cell-derived cardiomyocytes (iPSC-CMs) generated from patients with inherited forms of cardiomyopathies offer a unique platform to study the disease

mechanisms in physiologically relevant cells and tissues.[12,13] A few RASopathy-linked iPSC-CM models had been described, including for variants in *PTPN11*, *RAF1*, *BRAF*, and *MRAS*.[14–17] In line, we had recently added novel information as to the role of *LZTR1*-truncating variants in NS pathophysiology.[10] In the present study, we aimed to investigate the molecular, cellular, and functional consequences of a specific recessive missense variant $LZTR1^{L580P}$ by utilizing patient-derived and CRISPR-corrected iPSC-CMs. We could show that $LZTR1^{L580P}$ in homozygous state results in aberrant polymerization causing LZTR1 dysfunction, marked increase of RAS GTPase levels, and cellular hypertrophy. Further, uni- and bi-allelic genetic correction of the missense variant by CRISPR/Cas9 technology rescued the cellular phenotype, indicating that correction of one allele is sufficient to restore the cardiac pathophysiology, thereby providing proof-of-concept for future personalized CRISPR-based gene therapies.

Results

$LZTR1^{L580P}$ is causative for recessive Noonan syndrome

A 17-year old male patient presenting a HCM, stress-induced cardiac arrhythmias, pectus excavatum and facial anomalies was referred to our clinic and based on the combination of symptoms the clinical diagnosis of Noonan syndrome was given (Figure 1A). The patient was born to a consanguineous couple and both parents showed neither apparent clinical symptoms nor distinctive NS-specific features. Whole exome sequencing followed by detailed variant analysis detected one highly interesting, homozygous variant in *LZTR1*. Both parents were heterozygous carriers and the variant was not present in any current database of human genetic variations including the >250,000 alleles of gnomAD database. The homozygous missense variant, c.1739T>C, was located in exon 15 of the *LZTR1* gene and leads to the substitution of an evolutionary conserved leucine at the amino acid position 580 by proline (p.Leu580Pro,

p.L580P). The variant was predicted as likely causative by computational predictions.

To elucidate the molecular and functional consequences of the *LZTR1*^{L580P} missense variant, we generated iPSCs from the patient's skin fibroblasts using integration-free reprograming methods and subsequently utilized CRISPR/Cas9 genome editing to engineer gene variant-corrected iPSC lines (Figure 1B). For genetic correction of the patient-specific iPSCs, the CRISPR guide RNA was designed to specifically target the mutated sequence in exon 15 of the *LZTR1* gene. Further, the ribonucleoprotein-based CRISPR/Cas9 complex was combined with a single-stranded oligonucleotide serving as template for homology-directed repair (Figure 1C). Upon transfection, cells were singularized and individual clones were screened for successful editing to identify heterozygously corrected as well as homozygously corrected iPSC clones, LZTR1$^{corr\text{-}het}$ and LZTR1$^{corr\text{-}hom}$, respectively (Figure 1D). Molecular karyotyping of the edited iPSC clones confirmed chromosomal stability after genome editing and passaging (Figure 1E). As expected for individuals born to consanguineous parents, patient-specific as well as CRISPR-corrected iPSCs demonstrated a noticeable reduction of the overall heterozygosity using SNP-based genome-wide arrays, with around 30% of segments of the genome being assigned to regions of heterozygosity. Further, sequencing revealed no obvious off-target modifications by genome editing (Figure S1 in the supplement). Subsequently, patient-derived and CRISPR-corrected iPSCs were verified for pluripotency (Figure 1F-H). In addition to the patient-derived iPSC lines, iPSC lines from two unrelated healthy male donors, namely WT1 and WT11, were used as wild type (WT) controls in this study.

Homozygous LZTR1^{L580P} *causes accumulation of RAS GTPases*

At first, we aimed to investigate the impact of the identified homozygous *LZTR1*^{L580P} missense variant on the molecular mechanisms contributing to left ventricular hypertrophy in the patient.

Patient-specific, heterozygously and homozygously corrected, as well as two individual WT iPSC lines were differentiated into functional ventricular-like iPSC-CMs in feeder-free culture conditions,[18] and on day 60 of differentiation subjected to unbiased proteome analyses (Figure 2A). We identified more than 4,700 proteins in the samples from the individual groups. All samples showed a comparably high abundance of prominent cardiac markers including myosin heavy chain β (*MHY7*), cardiac troponin T (*TNNT2*), α-actinin (*ACTN2*), titin (*TTN*), and ventricular-specific myosin light chain 2 (*MYL2*), indicating equal cardiomyocyte content in the different cultures (Figure 2B). By comparing the proteome profiles of LZTR1^{L580P} and WT iPSC-CMs, we identified enhanced abundance of the RAS isoforms muscle RAS oncogene homolog (MRAS) and RIT1 in the patient's iPSC-CMs (Figure 2C). This finding is in agreement with our previous observation in *LZTR1*-truncating variant carriers[10] and confirms the pivotal role of LZTR1 in targeting various RAS isoforms for LZTR1-cullin 3 ubiquitin ligase complex-mediated ubiquitination, and degradation.[8,9] Further, it highlights that *LZTR1*^{L580P} results in protein loss-of-function, causing an accumulation of RAS proteins in the cells, providing molecular evidence for the causative nature of the missense variant. Strikingly, protein levels of the different RAS isoforms were normalized in both the heterozygously as well as the homozygously corrected iPSC-CMs, confirming that only one functional *LZTR1* allele is sufficient to regulate the protein pool of RAS GTPases in cardiomyocytes (Figure 2D-E). As anticipated, transcriptome analyses showed similar mRNA expression levels of the different RAS isoforms in the patient's and CRISPR-corrected iPSC lines, indicating a post-translational cause for the higher abundance of RAS proteins in LZTR1^{L580P} cultures (Figure S2 in the supplement). In contrast, the significantly elevated protein levels of the protein quality control-associated heat shock-related 70 kDa protein 2 (*HSPA2*) in the patient's cells in comparison to the WT and CRISPR-corrected cells were related to upregulation of gene expression, suggesting that HSPA2 is not directly targeted by LZTR1 for degradation.

To assess the correlation of the different proteomic profiles with respect to the disease-specific proteome signatures upon *LZTR1* deficiency, we performed a comparison analysis of the data sets from (1) LZTR1^{L580P} versus WT, (2) LZTR1$^{corr\text{-}het}$ versus LZTR1^{L580P}, and (3) LZTR1$^{corr\text{-}hom}$ versus LZTR1^{L580P}. We found 78 proteins being differentially regulated in all three data sets (Figure 2F). Here, a profound subset of proteins of the overlapping profile that was significantly higher abundant in the patient's cells, such as the MAPK-activated protein kinase RPS6KA3, was normalized after heterozygous and homozygous CRISPR-correction of the pathological *LZTR1* variant. Vice versa, numerous downregulated proteins in the patient samples were found to be elevated in the gene-edited iPSC-CMs. Further, we performed a Reactome pathway enrichment analysis to uncover dysregulated pathways and/or biological processes associated to *LZTR1*^{L580P}. The analysis indicated that differentially abundant proteins in patient-derived samples were enriched in critical cardiac-related biological processes, such as muscle contraction and extracellular matrix organization, as well as in cellular routes associated to metabolism (Figure 2G).

In agreement with the proteomic data, Western blot analysis confirmed the strong accumulation of MRAS, RIT1, and the classical RAS isoforms (HRAS, KRAS, and NRAS; detected by pan-RAS) in the LZTR1^{L580P} cultures, and further confirmed a normalization of RAS levels in the CRISPR-corrected isogenic iPSC-CMs to WT control levels (Figure 2H-K).

Collectively, these data demonstrate that the missense variant *LZTR1*^{L580P} in homozygosity resulted in protein loss-of-function causing an accumulation of RAS GTPases as the critical underlying disease mechanism in cardiomyocytes from the NS patient. In line, correction of the homozygous missense variant on at least one allele normalized the molecular pathology.

Homozygous LZTR1^{L580P} *provokes cardiomyocyte hypertrophy*

To elucidate the consequences of dysregulated RAS-MAPK signaling on the cellular characteristics of cardiomyocytes, we investigated the sarcomere homogeneity, the overall myofibril organization, and the cell size of the patient-derived iPSC-CMs, the CRISPR-corrected cells, as well as the WT controls at day 60 of differentiation (Figure 3A). Immunocytochemical staining of cardiac subtype-specific proteins revealed that all iPSC lines exhibit a well-organized sarcomeric organization with a pronounced striated expression of α-actinin and ventricular-specific MLC2V (Figure 3B). In order to analyze the homogeneity of sarcomeres in detail, we measured the distances between the sarcomeric Z-disks along individual myofibrils (Figure 3C). In agreement with the sarcomere length previously observed in neonatal and adult human hearts,[19] *LZTR1*-deficient as well as corrected and WT cells revealed a typical sarcomere length ranging from 1.7 to 2.2 µm with an average of approximately 1.9 µm across all iPSC lines (Figure 3D). As sarcomeric disarray has been frequently reported in other iPSC-CM models of both NS-associated and non-syndromic HCM,[15,20] we examined the myofibril organization in the individual iPSC-CMs stained for α-actinin by Fast Fourier Transform. The quantitative analysis did neither reveal any decrease of sarcomere regularity nor any pathological myofibril organization in $LZTR1^{L580P}$ cultures (Figure 3E). On the contrary, $LZTR1^{L580P}$ and CRISPR-corrected iPSC-CMs even demonstrated a slightly higher myofibril regularity compared to unrelated controls, indicating that the pathological gene variant has no severe impact on sarcomere structures.

As cardiomyocyte hypertrophy is a major hallmark of HCM, we further investigated the medium cell size of iPSC-CMs from all cell lines by utilizing our previously established assay to determine the cell size of iPSC-CMs in suspension.[10] Here, the patient's iPSC-CMs displayed a significant cellular enlargement compared to WT iPSC-CMs (Figure 3F). Strikingly, the hypertrophic phenotype was normalized in the CRISPR-corrected cells from both the $LZTR1^{corr\text{-}het}$ and the $LZTR1^{corr\text{-}hom}$ isogenic cultures. Moreover, and in line with the molecular

observations, heterozygous correction of the pathological variant was sufficient to significantly reduce cellular hypertrophy.

In summary, the patient's iPSC-CMs harboring the homozygous missense variant *LZTR1*^{L580P} recapitulated the cardiomyocyte hypertrophy *in vitro*. Importantly, CRISPR-correction of the pathological variant was able to normalize the hypertrophic phenotype.

Homozygous LZTR1^{L580P} *does not compromise contractile function*

NS-associated HCM as well as inherited forms of non-syndromic HCM are frequently associated with contractile dysfunction and these patients are at risk for developing arrhythmias.[21,22] Hence, we generated engineered heart muscles (EHMs) from diseased, CRISPR-corrected, and WT iPSC-CMs enabling us to investigate the functional characteristics in a three-dimensional environment closer resembling the native conditions of the human heart muscle (Figure 4A).[23,24] Microscopically, all iPSC lines formed homogenous cardiac tissues without showing apparent cell line-dependent differences after six weeks of cultivation and maturation (Figure 4B). Optical measurements were performed to study beating rate, force of contraction, and contraction kinetics in spontaneously contracting EHMs (Figure 4C). In comparison to WT EHMs, a slightly increased spontaneous beat frequency was detected in the LZTR1^{L580P} EHMs (Figure 4D). Interestingly, all tissues reflected a robust beat rhythm and a very low beat-to-beat variability over the entire recording time, indicating that the diseased tissues do not provoke development of arrhythmic events (Figure 4E). Furthermore, no significant differences in force of contraction were identified (Figure 4F). In accordance with higher beat frequencies, significantly shorter contraction times, and relaxation times were observed in LZTR1^{L580P}-, LZTR1$^{corr\text{-}het}$- and the LZTR1$^{corr\text{-}hom}$-derived EHMs (Figure 4G,H).

However, since the altered kinetics were noticed in both diseased and CRISPR-corrected tissues, this rather suggested a mutation-independent effect.

Taken together, this functional data indicates that the missense variant *LZTR1*^{L580P} does not significantly impact the contractile function and rhythmogenesis of cardiomyocytes.

Homozygous LZTR1^{L580P} *induces polymerization of LZTR1-cullin 3 ubiquitin ligase complexes*

Considering the severe consequence of *LZTR1*^{L580P} on the molecular and cellular pathophysiology in cardiomyocytes, we aimed to determine the specific effect of this variant on protein structure, complex formation, as well as its subcellular localization. We were not able to visualize endogenous LZTR1 in our cell model, neither by testing of multiple commercial antibodies nor by n-terminal or c-terminal genetic tagging of the *LZTR1* gene locus. In order to circumvent these obstacles, we established ectopic expression of tagged *LZTR1* in WT iPSC-CMs at around day 60 of differentiation by lipofectamine-based plasmid transfection (Figure 5A). Besides *LZTR1*^{WT} and *LZTR1*^{L580P}, we screened the NS patient database[25] for additional missense variants classified as likely pathogenic or variant of uncertain significance and located in close proximity to *LZTR1*^{L580P} (within the BACK1 domain), and included these in our screening panel (Figure 5B). Of note, except for *LZTR1*^{L580P} and *LZTR1*^{E563Q},[7] none of the other variants had been reported to be present in homozygosity in *LZTR1*-associated NS. In addition, we also included a truncating variant *LZTR1*$^{\Delta BTB2\text{-}BACK2}$, lacking the entire BTB2-BACK2 domain, that mimicked the genotype of the two siblings described in our previous study.[10]

As previously observed in other cell types (such as HeLa[8] and HEK293[26]), LZTR1^{WT} presented as dotted pattern equally distributed throughout the cell (Figure 5C, Figure S3A in the supplement). A similar dotted appearance was observed for the variants LZTR1^{E563Q},

LZTR1^{I570T}, LZTR1^{V579M}, LZTR1^{E584K}, and LZTR1^{R619H}. As expected, the truncating variant LZTR1$^{\Delta BTB2\text{-}BACK2}$ showed a mislocalized homogeneous cytoplasmic distribution. Surprisingly, missense variant LZTR1^{L580P} formed large filaments within the cytoplasm (Figure 5C, Figure S3A in the supplement). To verify this initial finding, we co-expressed two differentially tagged *LZTR1* constructs and evaluated their overlap within the cells. In accordance, LZTR1^{L580P} appeared as large protein polymers, whereas LZTR1^{WT} remained speckle-like (Figure 5D). As *LZTR1^{L580P}* in heterozygous state did not induce a disease phenotype based on our clinical and our experimental evidence, we hypothesized that co-expression of LZTR1^{L580P} and LZTR1^{WT} might resolve the polymer chains. Strikingly, the LZTR1^{L580P}-induced filaments dispersed when co-expressed with the WT variant, implicating that the LZTR1 complexes exclusively assembled to large protein polymers when the specific *LZTR1^{L580P}* missense variant is present on both alleles (Figure 5E). To quantitatively analyze these observations, we established an automated image-based speckle/filament recognition and computation (Figure S3B in the supplement). Whereas LZTR1^{WT} displayed a mean speckle size of 0.9 µm, the mean filament length per cell in LZTR1^{L580P} amounted to 7.9 µm (Figure 5F). In line, co-expression of mutant and WT constructs, and vice versa, normalized the speckle size to 1.2 µm and 1.3 µm, respectively.

Next, we asked whether LZTR1 polymerization might potentially interfere with proper targeting of degradation substrate MRAS or binding of ubiquitin ligase cullin 3. Thus, we evaluated co-localization of WT and mutant LZTR1 with MRAS and cullin 3 in WT iPSC-CMs after co-transfection (Figure 5G). Whereas, MRAS and cullin 3 displayed a homogeneous cytoplasmic distribution when expressed alone, both LZTR1^{WT} and LZTR1^{L580P} led to recruitment of MRAS and cullin 3 to the speckles and protein polymers, respectively (Figure 5H,I).

In summary, our data provides evidence that the missense variant *LZTR1*^{L580P} induces a unique polymerization of the LZTR1-cullin 3 ubiquitin ligase complexes. Furthermore, although binding of cullin 3 and degradation targets is not severely impaired by the mutation, it indicates that polymerization compromises the proper function of the LZTR1 ubiquitination complexes.

Homozygous LZTR1^{L580P} *alters binding affinities of dimerization domains*

Based on previous studies, proteins from the BTB-BACK-Kelch domain family including LZTR1 are predicted to assemble in homo-dimers.[9,26,27] However, our current knowledge regarding the exact domains responsible for LZTR1 dimerization is limited. In order to identify a plausible explanation for the *LZTR1*^{L580P}-induced polymerization, we utilized ColabFold – an AlphaFold-based platform for the prediction of protein structures and homo- and heteromer complexes.[28] We used a homo-trimer configuration of the experimentally employed *LZTR1* variants (all within the BACK1 domain) and AlphaFold-multimer predicted five high-quality models each with an average predicted local distance difference test (a per-residue confidence metric) between 64.1 and 76.0. For all variants, we inspected the interaction between the chains through the predicted alignment error (PAE) generated by AlphaFold-multimer (Figure S4 in the supplement). Here, a low PAE indicates that the relative position and orientation of the positions x and y was correctly predicted – a measure indicating if interfacing residues were correctly predicted across chains. Based on these predictions, we compared the top-ranked models of each variant according to the predicted template modeling score, which corresponded to overall topological accuracy (Figure 6A). The top-ranked model for LZTR1^{WT} showed interaction as a homo-dimer via the BACK2-BACK2 domain, whereas the third LZTR1 protein remained monomeric (Figure 6A,B). We also observed the identical dimerization via the BACK2 domains for all other variants, except for LZTR1^{L580P}. In contrast, the top-ranked model for LZTR1^{L580P} predicted an interaction between all three chains, on the one hand via

the BACK2-BACK2 domain and on the other hand via the BACK1-BACK1 domain (Figure 6A,B).

Collectively, these *in silico* predictions suggest that LZTR1 typically forms homo-dimers via the BACK2 domains, and that the missense variant *LZTR1*^{L580P} alters the binding affinities of the BACK1 domain enabling formation of linear LZTR1 polymer chains via both dimerization domains, thereby providing a rationale for the molecular and cellular impairments in NS (Figure 6C).

Discussion

Both autosomal dominant and autosomal recessive forms of *LZTR1*-associated NS have been described presenting with a broad clinical spectrum and various phenotypic expression of symptoms. However, the mechanistic consequences of numerous of these mutations, mostly classified as variants of uncertain significance, are still under debate. In previous studies, we and others elucidated the role of LZTR1 as a critical negative regulator of the RAS-MAPK pathway by controlling the pool of RAS GTPases.[8–10,26,29] By using patient-derived iPSC-CMs from NS patients with biallelic truncating *LZTR1* variants, we could show that *LZTR1* deficiency results in accumulation of RAS levels, signaling hyperactivity, and cardiomyocyte hypertrophy.[10] Further, by genetically correcting one of the two affected alleles, we could show that one functional *LZTR1* allele is sufficient to maintain normal RAS-MAPK activity in cardiac cells. In contrast to the truncating variants, dominant *LZTR1* missense variants generally cluster in the Kelch motif. Based on heterologous expression systems, these dominant variants are considered to perturb recognition or binding of RAS substrates to the LZTR1 ubiquitination complex.[8,9,11,29] Much less is known about the functional relevance of recessive *LZTR1* missense variants, which are distributed over the entire protein. Detailed insights in the

underlying molecular and functional mechanisms of selective variants causing the severe cardiac phenotype in NS enable to gain insights into specific structure-function relations of LZTR1 and are crucial to facilitate the development of patient-specific therapies.

In this study, we diagnosed a patient with NS, who presented typical clinical features of NS including an early-onset HCM and confirmed this diagnosis on genetic level by the identification of the homozygous, causative variant c.1739T>C/p.L580P in *LZTR1* by whole exome sequencing. The variant is novel and was not described before in patients with NS and we classified $LZTR1^{L580P}$ as likely causative based on its absence in gnomAD and our computational prediction. Besides this *LZTR1* variant, no additional variants were detected in other NS-associated genes or novel RAS-associated candidate genes. By combining *in vitro* disease modeling using patient-specific and CRISPR/Cas9-corrected iPSC-CMs, with molecular and cellular phenotyping, as well as *in silico* structural modeling, we uncovered a unique $LZTR1^{L580P}$-specific disease mechanism provoking the cardiac pathology of NS. In detail, we found that a) $LZTR1^{L580P}$ is predicted to alter the binding affinity of the BACK1 dimerization domain facilitating the formation of linear LZTR1 protein chains; b) homozygous $LZTR1^{L580P}$ fosters the assembly of large polymers of LZTR1-cullin 3 ubiquitin ligase complexes; c) pathological polymerization results in LZTR1 complex dysfunction, accumulation of RAS GTPases and RAS-MAPK signaling hyperactivity; and d) increased signaling activity induces global changes of the proteomic landscape ultimately causing cellular hypertrophy. Importantly, correction of one allele – in line with co-expression of WT and mutant *LZTR1* transcripts – is sufficient to normalize the cardiac disease phenotype both on molecular and cellular level.

Based on recent publications, there is a broad consensus about the role of LZTR1 as an adaptor protein for the cullin 3 ubiquitin ligase complex targeting RAS proteins for ubiquitination and subsequent protein degradation.[8–11,26,29] In line with observations in other NS-associated genes

and mutations, *LZTR1* dysfunction and concomitant accumulation of RAS GTPases results in hyperactivation of RAS-MAPK signaling. However, it remains controversial, whether LZTR1 is able to recognize all members of the RAS GTPase family for degradation or whether there is a selective affinity towards particular isoforms. By using heterologous expression systems, LZTR1 interaction with the main highly conserved RAS isoforms HRAS, KRAS and NRAS was observed.[8,26,29] On the contrary, Castel and colleagues observed a selective binding of LZTR1 with RIT1 and MRAS, but not with HRAS, KRAS or NRAS.[9] Moreover, in homozygous *LZTR1* knockout mice elevated RIT1 protein levels were detected across different organs including brain, liver, and heart, whereas HRAS, KRAS, and NRAS levels (recognized by pan-RAS) remained unchanged.[30] By using global proteomics, we now provide further evidence that LZTR1 dysfunction in cardiomyocytes in particular causes severe accumulation of MRAS and RIT1 and, to a lower extent, upregulation of the other isoforms HRAS, KRAS and NRAS, although all isoforms are robustly expressed in this cell type. We conclude that based on gene expression data and overall protein levels, MRAS seems to be the most prominent RAS candidate in cardiomyocytes driving the signaling hyperactivity in these cells. These observations suggest that under endogenous expression levels, LZTR1 possesses a certain selectivity towards MRAS and RIT1, and a lower affinity to the main isoforms HRAS, KRAS and NRAS. However, we cannot exclude that there might be potential cell type-specific differences in LZTR1-RAS binding affinities.

Besides accumulation of RAS members, HSPA2 was strongly upregulated in *LZTR1*-deficient iPSC-CMs both on transcriptional as well as on protein level, suggesting that HSPA2 is not a direct substrate of LZTR1. In line, severely increased HSPA2 levels had been observed by us in NS iPSC-CMs with *LZTR1*-truncating variants,[10] in a *RAF1*-related NS iPSC-CM model,[15] as well as in iPSC-CMs from Fabry disease patients, a lysosomal storage disorder associated with cardiac involvement such as HCM and arrhythmias.[31] Moreover, a significant

cardiomyocyte-specific elevation of HSPA2 was also observed in HCM tissue from patients.[32,33] A heat shock protein 70-based therapy has been shown to reverse lysosomal pathology,[34] whereas deletion of these gene members was assumed to induce cardiac dysfunction and development of cardiac hypertrophy.[35] As a member of the large group of chaperones, HSPA2 is known to have a dual function in cells: to mediate disaggregation and refolding of misfolded proteins as well as to assist in protein degradation via the ubiquitin-proteasome system or the lysosome-mediated autophagy.[36,37] This suggests that HSPA2 upregulation might be a cardio-protective adaptive response of the hypertrophic cardiomyocytes to cope with *LZTR1*^{L580P}-induced RAS accumulation (and potentially also with LZTR1 polymerization), by regulating the quality control mechanisms for protein degradation.

Major hallmarks of pathological cardiac hypertrophy include impaired cardiac function, changes in extracellular matrix composition, and fibrosis, as well as metabolic reprogramming and mitochondrial dysfunction.[38] In accordance, the proteomic disease signature of patient-derived iPSC-CM cultures revealed impairments in muscle contraction, extracellular matrix organization, and metabolism, all crucial for proper cardiomyocyte function. Furthermore, *LZTR1*^{L580P}-derived iPSC-CMs recapitulated the patient's hypertrophic phenotype reflected by cellular enlargement. Strikingly, both the molecular profile as well as cellular hypertrophy were resolved upon CRISPR-correction of the missense variant. Interestingly, no myofibrillar disarray was observed in our cell model. However, the presence of myofibril disarray in NS remains controversial: whereas structural defects were described in *RAF1*-associated iPSC models,[15,39] we and others did not observe any impact on sarcomere structures or myofibril organization in *LZTR1*-related, *PTPN11*-related, and *BRAF*-related iPSC-CMs,[10,14,16] implying potential genotype-dependent differences in the manifestation of myofibril disassembly in NS.

Missense variants in *LZTR1* located within the Kelch domain are predicted to affect substrate recognition, whereas missense variants in the BTB-BACK domain are assumed to impair either

binding of cullin 3, proper homo-dimerization, or correct subcellular localization. Several studies could provide proof that dominantly acting Kelch domain variants perturb recognition of RAS substrates, but do not affect LZTR1 complex stability or subcellular localization.[8,9,11,29,40] Vice versa, BTB-BACK missense variants showed no influence on RIT1 binding.[9,40] However, variants located in the BTB1 or the BTB2 domain, such as *LZTR1*^{V456G}, *LZTR1*^{R466Q}, *LZTR1*^{P520L}, and *LZTR1*^{R688C}, caused a subcellular mislocalization from defined speckles to a diffuse cytoplasmic distribution, similar to the findings obtained from truncating *LZTR1* variants.[8,29] In addition to these distinct pathological consequences from different variants analyzed so far, we now provide evidence for an alternative disease mechanism unique to BACK1 domain-located *LZTR1*^{L580P}: ectopic expression of *LZTR1*^{L580P} in iPSC-CMs caused a pathological polymerization of LZTR1 ubiquitination complexes. Moreover, it triggered a re-localization of MRAS and cullin 3 to the polymer chains, hence, binding probabilities to substrates and interaction partners were not significantly affected by the mutation. This remarkable phenotype was not observed for any other variant within the BACK1 domain. Notably, ectopic co-expression of *LZTR1*^{L580P} and *LZTR1*^{WT} alleviated the polymerization, indicating that the assembly of LZTR1 polymer chains exclusively occurs if the mutated proteins are present at homozygous state. Strikingly, an oligomerization of another BTB-BACK family member had been reported previously: Marzahn and colleagues revealed that dimers from the cullin 3 ubiquitin ligase substrate adaptor SPOP (harboring only one BTB-BACK domain) self-associate into linear higher-order oligomers via BACK domain dimerization.[41] These SPOP oligomers assembled in membrane-less cellular bodies, visualized as nuclear speckles, and it was proposed that the speckles might be important hotspots of ubiquitination. Based on these findings and our data, we propose that LZTR1 complexes concentrate in cellular speckles (either as dimers or as oligomers) to form subcellular clusters for efficient

ubiquitination and degradation of RAS proteins. However, *LZTR1*^{L580P}-induced polymerization of these complexes compromises regular function, leading to accumulation of substrates.

Our knowledge about the particular domains responsible for LZTR1 homo-dimerization is still incomplete. Whereas Castel and colleagues proposed that the BTB1 and the BACK1 domain are required for dimerization,[9] Steklov et al. observed impaired assembly in a BACK2 domain mutated *LZTR1* variant.[29] Based on *in silico* modeling, we now propose that LZTR1 can dimerize either via the BACK2-BACK2 domains or via the BACK1-BACK1 domains. Although in LZTR1^{WT} the BACK2-BACK2 dimerization might be primarily utilized, changes in binding affinities of the BACK1 domain as a consequence of *LZTR1*^{L580P} facilitated tandem self-association of dimers to linear multimers. Strikingly, the *in silico* models for complex assembly of the different variants were consistent with the experimental data. However, this analysis must be taken with caution as the PAE signal across chains is overall weak and AlphaFold-multimer was not trained with single point variants in mind. Of note, dimer + monomer as well as trimer interactions (in diverse combinations, such as via BACK2-BACK2 and BACK1-BACK1 or via BACK2-BACK2-BACK2) had also been predicted for the other BACK1 variants as well as for WT in the lower-ranked models (Figure S4 in the supplement). As a next step, it would be interesting to see, if the trend stays consistent for complexes with more chains. However, due to technical prerequisites, we were currently not able to predict more than three chains.

So far, the relevance of certain *LZTR1* missense variants on the molecular and cellular processes had been investigated in heterologous expression systems, failing to faithfully represent human cardiac physiology. Our study demonstrates the potential of patient-specific iPSCs to model human diseases and to uncover variant-specific pathomechanisms, which might facilitate the development for early and more precise therapies. Despite the great advantages of this model system over other cellular models, iPSC-CMs possess certain limitations. As summarized by

several reports, iPSC-CMs are considered to be developmentally immature characterized by molecular and functional properties similar to fetal CMs.[23,42,43] Although we complemented our study by utilizing three-dimensional EHMs, these *in vitro* models are currently not able to entirely resemble the disease phenotype at organ level. Nevertheless, our investigations at single cell and tissue level proofed to be a valuable platform for uncovering disease-relevant signaling pathways, identifying novel therapeutic targets and studying the disease progression during cardiogenesis.

Taken together, this study uncovered a novel mechanism causing recessive NS, which is initiated by $LZTR1^{L580P}$-driven polymerization of LZTR1 ubiquitination complexes, provoking molecular and cellular impairments associated with cardiac hypertrophy. Moreover, CRISPR-correction of the missense variant on one allele was sufficient to rescue the phenotype, thereby providing proof-of-concept for a sustainable therapeutic approach.

Materials and methods

Ethical approval

The study was approved by the Ethics Committee of the University Medical Center Göttingen (approval number: 10/9/15) and carried out in accordance with the approved guidelines. Written informed consent was obtained from all participants or their legal representatives prior to the participation in the study.

Whole exome sequencing

Whole exome sequencing on genomic DNA of the patient was performed using the SureSelect Human All Exon V6 kit (Agilent) on an Illumina HiSeq 4000 sequencer. The “Varbank 2.0” pipeline of the Cologne Center for Genomics (CCG) was used to analyze and interpret the

exome data, as previously described.[10] Co-segregation analysis was performed in the family. Computational predictions for the pathogenicity of the variant were performed using MutationTaster (https://www.mutationtaster.org/), SIFT (https://sift.bii.a-star.edu.sg/), and PolyPhen-2 (http://genetics.bwh.harvard.edu/pph2/).

Generation and culture of human iPSCs

Human iPSC lines from two healthy donors, from an NS patient with a pathological missense variant in *LZTR1* (NM_006767.4: c.1739T>C/p.L580P; ClinVar: RCV000677201.1), as well as heterozygous and homozygous CRISPR/Cas9-corrected iPSC lines were used in this study. Wild type iPSC lines UMGi014-C clone 14 (isWT1.14, here abbreviated as WT1) and UMGi130-A clone 8 (isWT11.8, here abbreviated as WT11) were generated from dermal fibroblasts and peripheral blood mononuclear cells from two male donors, respectively, using the integration-free Sendai virus and described previously.[44,45] Patient-specific iPSC line UMGi137-A clone 2 (isNoonSf1.2, here abbreviated as $LZTR1^{L580P}$) was generated from patient's dermal fibroblasts using the integration-free Sendai virus according manufacturer's instructions with modifications, as previously described.[10] Genetic correction of the pathological gene variant in the patient-derived iPSC line UMGi137-A clone 2 was performed using ribonucleoprotein-based CRISPR/Cas9 using crRNA/tracrRNA and Hifi SpCas9 (IDT DNA technologies) by targeting exon 15 of the *LZTR1* gene, as previously described.[10] The guide RNA target sequence was (PAM in bold): 5'-GCGGCACTCTCGCACACAAC **CGG**-3'. For homology-directed repair, a single-stranded oligonucleotide with 45-bp homology arms was used. After automated clonal singularization using the single cell dispenser CellenOne (Cellenion/Scienion) in StemFlex medium (Thermo Fisher Scientific), successful genome editing was identified by Sanger sequencing and the CRISPR-corrected isogenic iPSC lines UMGi137-A-1 clone D8 (isNoonSf1-corr.D8, here abbreviated as $L580P^{corr\text{-}het}$) and UMGi137-

A-1 clone D1 (isNoonSf1-corr.D1, here abbreviated as L580P$^{corr-hom}$) were established. Newly generated iPSC lines were maintained on Matrigel-coated (growth factor reduced, BD Biosciences) plates, passaged every 4-6 days with Versene solution (Thermo Fisher Scientific) and cultured in StemMACS iPS-Brew XF medium (Miltenyi Biotec) supplemented with 2 µM Thiazovivin (Merck Millipore) on the first day after passaging with daily medium change for at least ten passages before being used for molecular karyotyping, pluripotency characterization, and differentiation experiments. Pluripotency analysis via immunocytochemistry and flow cytometry was performed, as previously described.[10] For molecular karyotyping, genomic DNA of iPSC clones was sent for genome-wide analysis via Illumina BeadArray (Life&Brain, Germany). Digital karyotypes were analyzed in GenomeStudio v2.0 software (Illumina). For off-target screening, the top five predicted off-target regions for the respective guide RNA ranked by the CFD off-target score using CRISPOR[46] were analyzed by Sanger sequencing. Human iPSCs and iPSC-derivatives were cultured in feeder-free and serum-free culture conditions in a humidified incubator at 37°C and 5% CO_2. All antibodies used for immunofluorescence and flow cytometry are listed in Table S1 in the supplement.

Cardiomyocyte differentiation of iPSCs and generation of engineered heart muscle

Human iPSC lines were differentiated into ventricular iPSC-CMs via WNT signaling modulation and subsequent metabolic selection, as previously described,[18] and cultivated in feeder-free and serum-free culture conditions until day 60 post-differentiation before being used for molecular and cellular experiments. Defined, serum-free EHMs were generated from iPSC-CMs around day 30 of differentiation and human foreskin fibroblasts (ATCC) at a 70:30 ratio according to previously published protocols.[24] Optical analysis of contractility and rhythm of spontaneously beating EHMs in a 48 well plate was performed between day 34 and day 42 of

culture using a custom-built setup with a high-speed camera by recording the movement of the two UV light-absorbing flexible poles. Contractility parameters of EHM recordings of at least 1 min recording time were analyzed via a custom-build script in MatLab (MathWorks). For each iPSC line, three individual differentiations were used for EHM casting.

Proteomics and Western blot analysis of iPSC-CMs

For proteomic analysis, iPSC-CMs were pelleted at day 60 of differentiation by scratching in RIPA buffer (Thermo Fisher Scientific) containing phosphatase and protease inhibitor (Thermo Fisher Scientific) and snap-frozen in liquid nitrogen. Cell pellets were reconstituted in 8 M urea/ 2 M thiourea solution (Sigma-Aldrich) and lysed by five freeze-thaw cycles at 30°C and 1.600 rpm. Protein containing supernatant was collected by centrifugation. Nucleic acid was degraded enzymatically with 0.125 U/µg benzonase (Sigma-Aldrich), and protein concentration was determined by Bradford assay (Bio-Rad). Five µg protein was processed for LC-MS/MS analysis, as previously described.[47] Briefly, protein was reduced (2.5 mM dithiothreitol, Sigma-Aldrich; 30 min at 37°C) and alkylated (10 mM iodacetamide, Sigma-Aldrich; 15 min at 37°C) before proteolytic digestion with LysC (enzyme to protein ratio 1:100, Promega) for 3 h and with trypsin (1:25, Promega) for 16 h both at 37°C. The reaction was stopped with 1% acetic acid (Sigma-Aldrich), and the peptide mixtures were desalted on C-18 reverse phase material (ZipTip µ-C18, Millipore). Eluted peptides were concentrated by evaporation under vacuum and subsequently resolved in 0.1% acetic acid / 2% acetonitrile containing HRM/iRT peptides (Biognosys) according to manufacturer's recommendation. LC-MS/MS analysis was performed in data-independent acquisition (DIA) mode using an Ultimate 3000 UPLC system coupled to an Exploris 480 mass spectrometer (Thermo Scientific). Peptides were separated on a 25 cm Accucore column (75 µm inner diameter, 2.6 µm, 150 A, C18) at a flow rate of 300 nl/min in a linear gradient for 60 min. Spectronaut software

(Biognosys) was used for the analysis of mass spectrometric raw data. For peptide and protein identification, the Direct DIA approach based on UniProt database limited to human entries was applied. Carbamidomethylation at cysteine was set as static modification, oxidation at methionine and protein N-terminal acetylation were defined as variable modifications, and up to two missed cleavages were allowed. Ion values were parsed when at least 20% of the samples contained high quality measured values. Peptides were assigned to protein groups and protein inference was resolved by the automatic workflow implemented in Spectronaut. Statistical data analysis was conducted using an in-house developed R tool and based on median-normalized ion peak area intensities. Methionine oxidized peptides were removed before quantification. Differential abundant proteins (p-value ≤ 0.05) were identified by the algorithm ROPECA[48] and application of the reproducibility-optimized peptide change averaging approach[49] applied on peptide level. Only proteins quantified by at least two peptides were considered for further analysis. Reactome pathway enrichment analysis was performed using the ClueGo plugin in Cytoscape. For each iPSC line, at least three individual differentiations were analyzed. For Western blot analysis, protein containing supernatant was collected by centrifugation. Protein concentration was determined by BCA assay (Thermo Fisher Scientific). Samples were denatured at 95°C for 5 min. 15 µg protein were loaded onto a 4-15% Mini-PROTEAN TGX Stain-Free precast gel (Bio-Rad). The protein was separated by sodium dodecyl sulfate-polyacrylamide gel electrophoresis (SDS-PAGE) by applying 200 V for 30 min. Post-running, TGX gels were activated via UV light application using the Trans-Blot Turbo transfer system (Bio-Rad). While blotting, proteins were transferred to a nitrocellulose membrane (25 V constant, 1.3 A for 7 min). Total protein amount was detected via the ChemiDoc XRS+ (Bio-Rad) system and used for protein normalization. After 1 h in blocking solution (5% milk in TBS-T, Sigma-Aldrich), membranes were incubated in primary antibody solution (1% milk in TBS-T) overnight. Membrane was washed trice with TBS-T before applying the secondary

antibody (1:10,000 in 1% milk in TBS-T) at RT for 1 h. After washing, signals were detected upon application of SuperSignal West Femto Maximum Sensitivity Substrat (Thermo Fisher Scientific). Image acquisition was performed with the ChemiDoc XRS+ (Bio-Rad) at the high-resolution mode. For protein quantification, ImageLab (Bio-Rad) was used and protein levels were first normalized to total protein and second to the corresponding WT samples on each blot. For each iPSC line, 8 individual differentiations were analyzed. All antibodies used for Western blot are listed in Table S1 in the supplement.

Real-time PCR analysis of iPSC-CMs

Pellets of iPSC-CMs at day 60 of differentiation were snap-frozen in liquid nitrogen and stored at -80°C. Total RNA was isolated using the NucleoSpin RNA Mini kit (Macherey-Nagel) according to manufacturer's instructions. 200 ng RNA was used for the first-strand cDNA synthesis by using the MULV Reverse Transcriptase and Oligo d(T)16 (Thermo Fisher Scientific). For real-time PCR, cDNA was diluted 1:1 with nuclease-free water (Promega). Quantitative real-time PCR reactions were carried out using the SYBR Green PCR master mix and ROX Passive Reference Dye (Bio-Rad) with Micro-Amp Optical 384-well plates, and the 7900HT fast real-time PCR system (Applied Biosystems) according to the manufacturer's instructions with the following parameters: 95°C for 10 min, followed by 40 cycles at 95°C for 15 s and 60°C for 1 min. Analysis was conducted using the ΔΔCT method and values were normalized to *GAPDH* gene expression and to WT controls. Primer sequences are listed in Table S2 in the supplement.

Analysis of sarcomere length and myofibril organization of iPSC-CMs

To analyze the sarcomere length and myofibril organization, iPSC-CMs were cultured on Matrigel-coated coverslips and fixed at day 60 of differentiation in 4% Roti-Histofix (Carl Roth) at RT for 10 min and blocked with 1% Bovine Serum Albumin (BSA; Sigma-Aldrich) in PBS (Thermo Fisher Scientific) overnight at 4°C. Primary antibodies were applied in 1% BSA and 0.1% Triton-X100 (Carl Roth) in PBS at 37°C for 1 h or at 4°C overnight. Secondary antibodies with minimal cross reactivity were administered in 1% BSA in PBS (Thermo Fisher Scientific) at RT for 1 h. Nuclei were stained with 8.1 µM Hoechst 33342 (Thermo Fisher Scientific) at RT for 10 min. Samples were mounted in Fluoromount-G (Thermo Fisher Scientific). Images were collected using the Axio Imager M2 microscopy system (Carl Zeiss) and Zen 2.3 software. For analysis of the sarcomere length, images with α-actinin staining of iPSC-CMs were evaluated using the SarcOptiM plugin in ImageJ (National Institutes of Health).[50] Here, three independent lines along different myofibrils within one cell were selected to calculate the mean sarcomere length per cell. For each iPSC line, three individual differentiations with 9-13 images per differentiation and two cells per image were analyzed. To analyze the myofibril organization, images with α-actinin staining of iPSC-CMs were processed using the Tubeness and Fast Fourier Transform plugins in ImageJ. Processed images were radially integrated using the Radial Profile Plot plugin in ImageJ and the relative amplitude of the first-order peak in the intensity profile as a measure of sarcomere and myofibril regularity was automatically analyzed using LabChart (ADInstruments). For each iPSC line, three individual differentiations with 7-11 images per differentiation were analyzed. All antibodies used for immunofluorescence are listed in Table S1 in the supplement.

Analysis of cell size of iPSC-CMs

To study cellular hypertrophy, iPSC-CMs at day 60 of differentiation were analyzed for cell size in suspension, as previously described.[10] In brief, iPSC-CMs at day 50 of differentiation

were plated at a density of 2.5×10^5 cells per well on Matrigel-coated 12-well plates. At day 60 of differentiation, cells were singularized with StemPro Accutase Cell Dissociation Reagent (Thermo Fisher Scientific) and measured for cell diameter using the CASY cell counter system (OMNI Life Science). Each value represents a mean of 5×10^2 to 1.5×10^4 cells per measurement. To exclude cell debris and cell clusters, only values within a diameter range of 15-40 µm were selected. For each iPSC line, at least three individual differentiations with 3-5 replicates per differentiation were analyzed.

Ectopic expression of LZTR1 variants in iPSC-CMs

For ectopic expression studies, the human WT *LZTR1* coding sequence was synthesized (Genewiz/Azenta Life Sciences) and subcloned in *pcDNA3-HA-humanNEMO* (gift from Kunliang Guan, Addgene plasmid #13512) by exchanging the *NEMO* coding sequence. Additionally, the HA-tag was exchanged by a FLAG-tag by synthesis of the fragment and subcloning in *pcDNA3-HA-LZTR1-WT* (Genewiz/Azenta Life Sciences). Patient-specific mutations were introduced into *pcDNA3-HA-LZTR1-WT* and *pcDNA3-FLAG-LZTR1-WT* using mutagenesis PCR. The plasmids *pCMV6-MRAS-Myc-DDK* (Origene, #RC212259) and *pcDNA3-Myc-CUL3* (gift from Yue Xiong, Addgene plasmid #19893) were used for co-expression experiments. Plasmid DNA was isolated via the endotoxin-free NucleoBond Xtra Midi Plus EF kit (Macherey-Nagel). For transfection, WT1 iPSC-CMs cultured on Matrigel-coated 4-well chamber slides at a density of 7×10^4 cells per well were transfected at day 60 of differentiation with the respective plasmids using Lipofectamine Stem Transfection Reagent (Thermo Fisher Scientific) according to manufacturer's instructions with 700 ng per plasmid. After 24 h post-transfection, cells were fixed, stained, and imaged as described above. To quantitatively analyze speckle size and filament length, a custom-build pipeline in CellProfiler (BROAD institute) was applied. For each *LZTR1* variant, plasmid transfections were performed

in at least three replicates. All antibodies used for immunofluorescence are listed in Table S1 in the supplement. All plasmids used are listed in Table S3 in the supplement.

In silico prediction of protein structures and multimer complexes

Homo-trimer configurations of the different *LZTR1* variants were predicted using ColabFold (version 02c53)[28] and AlphaFold-multimer v2[51] with 6 recycles and no templates on an A5000 GPU with 24 GBs of RAM and repeated twice. The five predicted models for each variant were ranked according to the predicted template modeling score and interactions between the chains were inspected through the predicted alignment error generated by AlphaFold-multimer.

Statistics

Data are presented as the mean ± standard error of the mean, unless otherwise specified. Statistical comparisons were performed using the D'Agostino-Pearson normality test and the nonparametric Kruskal-Wallis test followed by Dunn correction in Prism 8 (GraphPad). Results were considered statistically significant when the p-value was ≤ 0.05.

Data and biomaterial availability

The mass spectrometry proteomics data have been deposited to the ProteomeXchange Consortium via the PRIDE partner repository (https://www.proteomexchange.org/) with the identifiers PXD038425 and PXD038417. All human iPSC lines used in this study are deposited in the stem cell biobank of the University Medical Center Göttingen and are available for research use upon request.

Acknowledgements

We thank Laura Cyganek, Yvonne Hintz, Nadine Gotzmann, Lisa Schreiber, and Yvonne Wedekind (Stem Cell Unit, University Medical Center Göttingen), Branimir Berečić, Tim Meyer and Malte Tiburcy (Institute of Pharmacology and Toxicology, University Medical Center Göttingen), and Anja Wiechert and Manuela Gesell Salazar (Interfaculty Institute of Genetics and Functional Genomics, University Medicine Greifswald) for excellent technical assistance.

This work was supported by the German Research Foundation (DFG): project number 417880571 to L.C.; project number 501985000 to L.C.; project number 193793266, Collaborative Research Centre 1002, C04, D01, D02 and S01 to W.H.Z., G.H., B.W. and L.C.; project number 390729940, Germany's Excellence Strategy - EXC 2067/1 to A.V.B., G.H., W.H.Z., B.W. and L.C.; by the Else Kröner Fresenius Foundation: project number 2019_A75 to L.C.; by the German Federal Ministry of Education and Research (BMBF)/ German Center for Cardiovascular Research (DZHK) to E.H., G.H., W.H.Z., B.W. and L.C.; and by the Leducq Foundation: project number 20CVD04 to W.H.Z.

Author contributions

L.C. designed the study. L.C. and A.V.B. designed the experiments. A.V.B., O.G.G., E.H., M.S., L.B., H.S., M.K., J.A., F.M., and L.C. performed the experiments and analyzed the data. G.H., W.H.Z. and B.W. gave technical support and conceptual advice. L.C. and A.V.B. wrote and edited the manuscript.

Conflict of interest disclosures

The authors declare that they have no conflict of interest.

References

1. Roberts AE, Allanson JE, Tartaglia M, Gelb BD. Noonan syndrome. *Lancet*. 2013;381:333–342. doi: 10.1016/S0140-6736(12)61023-X
2. Linglart L, Gelb BD. Congenital heart defects in Noonan syndrome: Diagnosis, management, and treatment. *Am J Med Genet C Semin Med Genet*. 2020;184:73–80. doi: 10.1002/ajmg.c.31765
3. Hickey EJ, Mehta R, Elmi M, Asoh K, McCrindle BW, Williams WG, Manlhiot C, Benson L. Survival implications: hypertrophic cardiomyopathy in Noonan syndrome. Hypertrophic cardiomyopathy in Noonan syndrome. *Congenit Heart Dis*. 2011;6:41–47. doi: 10.1111/j.1747-0803.2010.00465.x
4. Wilkinson JD, Lowe AM, Salbert BA, Sleeper LA, Colan SD, Cox GF, Towbin JA, Connuck DM, Messere JE, Lipshultz SE. Outcomes in children with Noonan syndrome and hypertrophic cardiomyopathy: a study from the Pediatric Cardiomyopathy Registry. A study from the Pediatric Cardiomyopathy Registry. *Am Heart J*. 2012;164:442–448. doi: 10.1016/j.ahj.2012.04.018
5. Aoki Y, Niihori T, Inoue S, Matsubara Y. Recent advances in RASopathies. *J Hum Genet*. 2016;61:33–39. doi: 10.1038/jhg.2015.114
6. Leoni C, Blandino R, Delogu AB, Rosa G de, Onesimo R, Verusio V, Marino MV, Lanza GA, Rigante D, Tartaglia M, Zampino G. Genotype-cardiac phenotype correlations in a large single-center cohort of patients affected by RASopathies: Clinical implications and literature review. *Am J Med Genet A*. 2022;188:431–445. doi: 10.1002/ajmg.a.62529
7. Johnston JJ, van der Smagt JJ, Rosenfeld JA, Pagnamenta AT, Alswaid A, Baker EH, Blair E, Borck G, Brinkmann J, Craigen W, Dung VC, Emrick L, Everman DB, van Gassen KL, Gulsuner S, Harr MH, Jain M, Kuechler A, Leppig KA, McDonald-McGinn DM, Can NTB, Peleg A, Roeder ER, Rogers RC, Sagi-Dain L, Sapp JC, Schäffer AA, Schanze D, Stewart H, Taylor JC, Verbeek NE, Walkiewicz MA, Zackai EH, Zweier C, Zenker M, Lee B, Biesecker LG. Autosomal recessive Noonan syndrome associated with biallelic LZTR1 variants. *Genet Med*. 2018;20:1175–1185. doi: 10.1038/gim.2017.249
8. Bigenzahn JW, Collu GM, Kartnig F, Pieraks M, Vladimer GI, Heinz LX, Sedlyarov V, Schischlik F, Fauster A, Rebsamen M, Parapatics K, Blomen VA, Müller AC, Winter GE, Kralovics R, Brummelkamp TR, Mlodzik M, Superti-Furga G. LZTR1 is a regulator of RAS ubiquitination and signaling. *Science*. 2018;362:1171–1177. doi: 10.1126/science.aap8210

9. Castel P, Cheng A, Cuevas-Navarro A, Everman DB, Papageorge AG, Simanshu DK, Tankka A, Galeas J, Urisman A, McCormick F. RIT1 oncoproteins escape LZTR1-mediated proteolysis. *Science*. 2019;363:1226–1230. doi: 10.1126/science.aav1444
10. Hanses U, Kleinsorge M, Roos L, Yigit G, Li Y, Barbarics B, El-Battrawy I, Lan H, Tiburcy M, Hindmarsh R, Lenz C, Salinas G, Diecke S, Müller C, Adham I, Altmüller J, Nürnberg P, Paul T, Zimmermann W-H, Hasenfuss G, Wollnik B, Cyganek L. Intronic CRISPR Repair in a Preclinical Model of Noonan Syndrome-Associated Cardiomyopathy. *Circulation*. 2020;142:1059–1076. doi: 10.1161/CIRCULATIONAHA.119.044794
11. Motta M, Fidan M, Bellacchio E, Pantaleoni F, Schneider-Heieck K, Coppola S, Borck G, Salviati L, Zenker M, Cirstea IC, Tartaglia M. Dominant Noonan syndrome-causing LZTR1 mutations specifically affect the Kelch domain substrate-recognition surface and enhance RAS-MAPK signaling. *Hum Mol Genet*. 2019;28:1007–1022. doi: 10.1093/hmg/ddy412
12. Sayed N, Liu C, Wu JC. Translation of Human-Induced Pluripotent Stem Cells: From Clinical Trial in a Dish to Precision Medicine. From Clinical Trial in a Dish to Precision Medicine. *Journal of the American College of Cardiology*. 2016;67:2161–2176. doi: 10.1016/j.jacc.2016.01.083
13. van Mil A, Balk GM, Neef K, Buikema JW, Asselbergs FW, Wu SM, Doevendans PA, Sluijter JPG. Modelling inherited cardiac disease using human induced pluripotent stem cell-derived cardiomyocytes: progress, pitfalls, and potential. *Cardiovasc Res*. 2018;114:1828–1842. doi: 10.1093/cvr/cvy208
14. Meier AB, Raj Murthi S, Rawat H, Toepfer CN, Santamaria G, Schmid M, Mastantuono E, Schwarzmayr T, Berutti R, Cleuziou J, Ewert P, Görlach A, Klingel K, Laugwitz K-L, Seidman CE, Seidman JG, Moretti A, Wolf CM. Cell cycle defects underlie childhood-onset cardiomyopathy associated with Noonan syndrome. *iScience*. 2022;25:103596. doi: 10.1016/j.isci.2021.103596
15. Jaffré F, Miller CL, Schänzer A, Evans T, Roberts AE, Hahn A, Kontaridis MI. Inducible Pluripotent Stem Cell-Derived Cardiomyocytes Reveal Aberrant Extracellular Regulated Kinase 5 and Mitogen-Activated Protein Kinase Kinase 1/2 Signaling Concomitantly Promote Hypertrophic Cardiomyopathy in RAF1-Associated Noonan Syndrome. *Circulation*. 2019;140:207–224. doi: 10.1161/CIRCULATIONAHA.118.037227
16. Josowitz R, Mulero-Navarro S, Rodriguez NA, Falce C, Cohen N, Ullian EM, Weiss LA, Rauen KA, Sobie EA, Gelb BD. Autonomous and Non-autonomous Defects Underlie

Hypertrophic Cardiomyopathy in BRAF-Mutant hiPSC-Derived Cardiomyocytes. *Stem cell reports*. 2016;7:355–369. doi: 10.1016/j.stemcr.2016.07.018

17. Higgins EM, Bos JM, Dotzler SM, John Kim CS, Ackerman MJ. MRAS Variants Cause Cardiomyocyte Hypertrophy in Patient-Specific Induced Pluripotent Stem Cell-Derived Cardiomyocytes: Additional Evidence for MRAS as a Definitive Noonan Syndrome-Susceptibility Gene. *Circ Genom Precis Med*. 2019;12:e002648. doi: 10.1161/CIRCGEN.119.002648
18. Kleinsorge M, Cyganek L. Subtype-Directed Differentiation of Human iPSCs into Atrial and Ventricular Cardiomyocytes. *STAR protocols*. 2020;1:100026. doi: 10.1016/j.xpro.2020.100026
19. Lemcke H, Skorska A, Lang CI, Johann L, David R. Quantitative Evaluation of the Sarcomere Network of Human hiPSC-Derived Cardiomyocytes Using Single-Molecule Localization Microscopy. *Int J Mol Sci*. 2020;21. doi: 10.3390/ijms21082819
20. Mosqueira D, Mannhardt I, Bhagwan JR, Lis-Slimak K, Katili P, Scott E, Hassan M, Prondzynski M, Harmer SC, Tinker A, Smith JGW, Carrier L, Williams PM, Gaffney D, Eschenhagen T, Hansen A, Denning C. CRISPR/Cas9 editing in human pluripotent stem cell-cardiomyocytes highlights arrhythmias, hypocontractility, and energy depletion as potential therapeutic targets for hypertrophic cardiomyopathy. *Eur Heart J*. 2018;39:3879–3892. doi: 10.1093/eurheartj/ehy249
21. Levin MD, Saitta SC, Gripp KW, Wenger TL, Ganesh J, Kalish JM, Epstein MR, Smith R, Czosek RJ, Ware SM, Goldenberg P, Myers A, Chatfield KC, Gillespie MJ, Zackai EH, Lin AE. Nonreentrant atrial tachycardia occurs independently of hypertrophic cardiomyopathy in RASopathy patients. *Am J Med Genet A*. 2018;176:1711–1722. doi: 10.1002/ajmg.a.38854
22. Maron BJ, Desai MY, Nishimura RA, Spirito P, Rakowski H, Towbin JA, Rowin EJ, Maron MS, Sherrid MV. Diagnosis and Evaluation of Hypertrophic Cardiomyopathy: JACC State-of-the-Art Review. *J Am Coll Cardiol*. 2022;79:372–389. doi: 10.1016/j.jacc.2021.12.002
23. Cyganek L, Tiburcy M, Sekeres K, Gerstenberg K, Bohnenberger H, Lenz C, Henze S, Stauske M, Salinas G, Zimmermann W-H, Hasenfuss G, Guan K. Deep phenotyping of human induced pluripotent stem cell-derived atrial and ventricular cardiomyocytes. *JCI Insight*. 2018;3:99941. doi: 10.1172/jci.insight.99941

24. Tiburcy M, Meyer T, Liaw NY, Zimmermann W-H. Generation of Engineered Human Myocardium in a Multi-well Format. *STAR protocols*. 2020;1:100032. doi: 10.1016/j.xpro.2020.100032
25. NSEuroNet.com. https://nseuronet.com/php/. Accessed December 29, 2022
26. Abe T, Umeki I, Kanno S-I, Inoue S, Niihori T, Aoki Y. LZTR1 facilitates polyubiquitination and degradation of RAS-GTPases. *Cell Death Differ*. 2020;27:1023–1035. doi: 10.1038/s41418-019-0395-5
27. Canning P, Cooper CDO, Krojer T, Murray JW, Pike ACW, Chaikuad A, Keates T, Thangaratnarajah C, Hojzan V, Marsden BD, Gileadi O, Knapp S, Delft F von, Bullock AN. Structural basis for Cul3 protein assembly with the BTB-Kelch family of E3 ubiquitin ligases. *J Biol Chem*. 2013;288:7803–7814. doi: 10.1074/jbc.M112.437996
28. Mirdita M, Schütze K, Moriwaki Y, Heo L, Ovchinnikov S, Steinegger M. ColabFold: making protein folding accessible to all. *Nat Methods*. 2022;19:679–682. doi: 10.1038/s41592-022-01488-1
29. Steklov M, Pandolfi S, Baietti MF, Batiuk A, Carai P, Najm P, Zhang M, Jang H, Renzi F, Cai Y, Abbasi Asbagh L, Pastor T, Troyer M de, Simicek M, Radaelli E, Brems H, Legius E, Tavernier J, Gevaert K, Impens F, Messiaen L, Nussinov R, Heymans S, Eyckerman S, Sablina AA. Mutations in LZTR1 drive human disease by dysregulating RAS ubiquitination. *Science*. 2018;362:1177–1182. doi: 10.1126/science.aap7607
30. Cuevas-Navarro A, Rodriguez-Muñoz L, Grego-Bessa J, Cheng A, Rauen KA, Urisman A, McCormick F, Jimenez G, Castel P. Cross-species analysis of LZTR1 loss-of-function mutants demonstrates dependency to RIT1 orthologs. *Elife*. 2022;11. doi: 10.7554/eLife.76495
31. Birket MJ, Raibaud S, Lettieri M, Adamson AD, Letang V, Cervello P, Redon N, Ret G, Viale S, Wang B, Biton B, Guillemot J-C, Mikol V, Leonard JP, Hanley NA, Orsini C, Itier J-M. A Human Stem Cell Model of Fabry Disease Implicates LIMP-2 Accumulation in Cardiomyocyte Pathology. *Stem Cell Reports*. 2019;13:380–393. doi: 10.1016/j.stemcr.2019.07.004
32. Dorsch LM, Schuldt M, dos Remedios CG, Schinkel AFL, Jong PL de, Michels M, Kuster DWD, Brundel BJJM, van der Velden J. Protein Quality Control Activation and Microtubule Remodeling in Hypertrophic Cardiomyopathy. *Cells*. 2019;8. doi: 10.3390/cells8070741
33. Pei J, Schuldt M, Nagyova E, Gu Z, El Bouhaddani S, Yiangou L, Jansen M, Calis JJA, Dorsch LM, Blok CS, van den Dungen NAM, Lansu N, Boukens BJ, Efimov IR, Michels

M, Verhaar MC, Weger R de, Vink A, van Steenbeek FG, Baas AF, Davis RP, Uh HW, Kuster DWD, Cheng C, Mokry M, van der Velden J, Asselbergs FW, Harakalova M. Multi-omics integration identifies key upstream regulators of pathomechanisms in hypertrophic cardiomyopathy due to truncating MYBPC3 mutations. *Clin Epigenetics*. 2021;13:61. doi: 10.1186/s13148-021-01043-3

34. Kirkegaard T, Gray J, Priestman DA, Wallom K-L, Atkins J, Olsen OD, Klein A, Drndarski S, Petersen NHT, Ingemann L, Smith DA, Morris L, Bornæs C, Jørgensen SH, Williams I, Hinsby A, Arenz C, Begley D, Jäättelä M, Platt FM. Heat shock protein-based therapy as a potential candidate for treating the sphingolipidoses. *Sci. Transl. Med.* 2016;8:355ra118. doi: 10.1126/scitranslmed.aad9823
35. Kim Y-K, Suarez J, Hu Y, McDonough PM, Boer C, Dix DJ, Dillmann WH. Deletion of the inducible 70-kDa heat shock protein genes in mice impairs cardiac contractile function and calcium handling associated with hypertrophy. *Circulation*. 2006;113:2589–2597. doi: 10.1161/CIRCULATIONAHA.105.598409
36. Ranek MJ, Stachowski MJ, Kirk JA, Willis MS. The role of heat shock proteins and co-chaperones in heart failure. *Philos Trans R Soc Lond , B, Biol Sci*. 2018;373. doi: 10.1098/rstb.2016.0530
37. Fernández-Fernández MR, Gragera M, Ochoa-Ibarrola L, Quintana-Gallardo L, Valpuesta JM. Hsp70 - a master regulator in protein degradation. *FEBS Letters*. 2017;591:2648–2660. doi: 10.1002/1873-3468.12751
38. Nakamura M, Sadoshima J. Mechanisms of physiological and pathological cardiac hypertrophy. *Nat Rev Cardiol*. 2018;15:387–407. doi: 10.1038/s41569-018-0007-y
39. Nakhaei-Rad S, Bazgir F, Dahlmann J, Busley AV, Buchholzer M, Haghighi F, Schänzer A, Hahn A, Kötter S, Schanze D, Anand R, Funk F, Borchardt A, Kronenbitter AV, Scheller J, Piekorz RP, Reichert AS, Volleth M, Wolf MJ, Cirstea IC, Gelb BD, Tartaglia M, Schmitt J, Krüger M, Kutschka I, Cyganek L, Zenker M, Kensah G, Ahmadian MR. Alteration of myocardial structure and function in RAF1-associated Noonan syndrome: Insights from cardiac disease modeling based on patient-derived iPSCs. *bioRxiv*. 2022. doi: 10.1101/2022.01.22.477319
40. Wang Y, Zhang J, Zhang P, Zhao Z, Huang Q, Yun D, Chen J, Chen H, Wang C, Lu D. LZTR1 inactivation promotes MAPK/ ERK pathway activation in glioblastoma by stabilizing oncoprotein RIT1. *bioRxiv*. 2020. doi: 10.1101/2020.03.14.989954
41. Marzahn MR, Marada S, Lee J, Nourse A, Kenrick S, Zhao H, Ben-Nissan G, Kolaitis R-M, Peters JL, Pounds S, Errington WJ, Privé GG, Taylor JP, Sharon M, Schuck P, Ogden

SK, Mittag T. Higher-order oligomerization promotes localization of SPOP to liquid nuclear speckles. *EMBO J*. 2016;35:1254–1275. doi: 10.15252/embj.201593169

42. Karbassi E, Fenix A, Marchiano S, Muraoka N, Nakamura K, Yang X, Murry CE. Cardiomyocyte maturation: advances in knowledge and implications for regenerative medicine. *Nat Rev Cardiol*. 2020;17:341–359. doi: 10.1038/s41569-019-0331-x
43. Guo Y, Pu WT. Cardiomyocyte Maturation: New Phase in Development. *Circ Res*. 2020;126:1086–1106. doi: 10.1161/CIRCRESAHA.119.315862
44. Rössler U, Hennig AF, Stelzer N, Bose S, Kopp J, Søe K, Cyganek L, Zifarelli G, Ali S, Hagen M von der, Strässler ET, Hahn G, Pusch M, Stauber T, Izsvák Z, Gossen M, Stachelscheid H, Kornak U. Efficient generation of osteoclasts from human induced pluripotent stem cells and functional investigations of lethal CLCN7-related osteopetrosis. *J Bone Miner Res*. 2021;36:1621–1635. doi: 10.1002/jbmr.4322
45. Yousefi R, Fornasiero EF, Cyganek L, Montoya J, Jakobs S, Rizzoli SO, Rehling P, Pacheu-Grau D. Monitoring mitochondrial translation in living cells. *EMBO Rep*. 2021;22:e51635. doi: 10.15252/embr.202051635
46. Haeussler M, Schönig K, Eckert H, Eschstruth A, Mianné J, Renaud J-B, Schneider-Maunoury S, Shkumatava A, Teboul L, Kent J, Joly J-S, Concordet J-P. Evaluation of off-target and on-target scoring algorithms and integration into the guide RNA selection tool CRISPOR. *Genome Biol*. 2016;17:148. doi: 10.1186/s13059-016-1012-2
47. Zech ATL, Prondzynski M, Singh SR, Pietsch N, Orthey E, Alizoti E, Busch J, Madsen A, Behrens CS, Meyer-Jens M, Mearini G, Lemoine MD, Krämer E, Mosqueira D, Virdi S, Indenbirken D, Depke M, Salazar MG, Völker U, Braren I, Pu WT, Eschenhagen T, Hammer E, Schlossarek S, Carrier L. ACTN2 Mutant Causes Proteopathy in Human iPSC-Derived Cardiomyocytes. *Cells*. 2022;11. doi: 10.3390/cells11172745
48. Suomi T, Elo LL. Enhanced differential expression statistics for data-independent acquisition proteomics. *Sci Rep*. 2017;7:5869. doi: 10.1038/s41598-017-05949-y
49. Seyednasrollah F, Rantanen K, Jaakkola P, Elo LL. ROTS: reproducible RNA-seq biomarker detector-prognostic markers for clear cell renal cell cancer. *Nucleic Acids Res*. 2016;44:e1. doi: 10.1093/nar/gkv806
50. Pasqualin C, Gannier F, Yu A, Malécot CO, Bredeloux P, Maupoil V. SarcOptiM for ImageJ: high-frequency online sarcomere length computing on stimulated cardiomyocytes. *Am J Physiol , Cell Physiol*. 2016;311:C277-83. doi: 10.1152/ajpcell.00094.2016

51. Evans R, O'Neill M, Pritzel A, Antropova N, Senior A, Green T, Žídek A, Bates R, Blackwell S, Yim J, Ronneberger O, Bodenstein S, Zielinski M, Bridgland A, Potapenko A, Cowie A, Tunyasuvunakool K, Jain R, Clancy E, Kohli P, Jumper J, Hassabis D. Protein complex prediction with AlphaFold-Multimer. *bioRxiv*. 2021. doi: 10.1101/2021.10.04.463034

Figure Legends

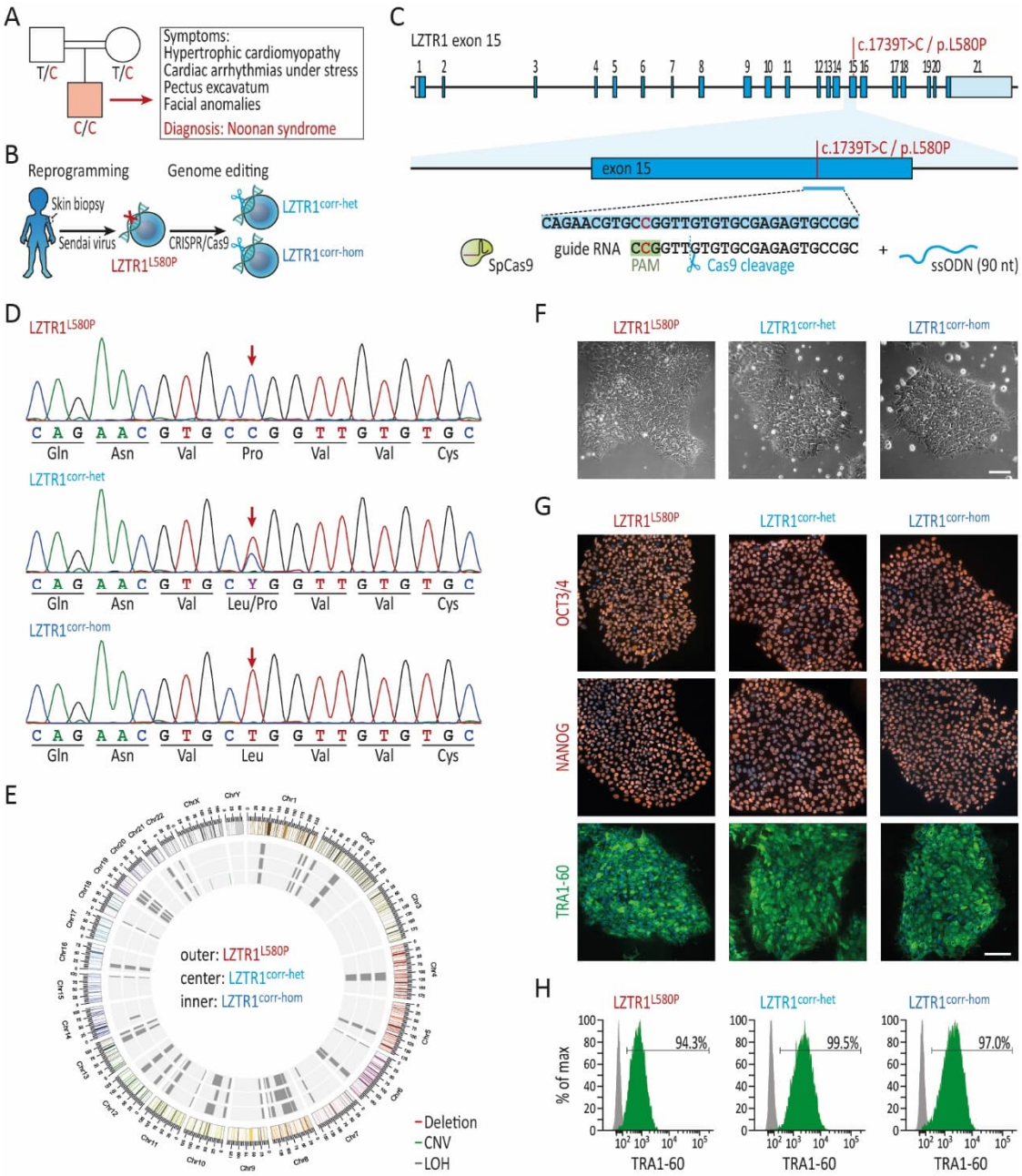

Figure 1: Generation of patient-specific and CRISPR-corrected iPSCs for disease modeling of recessive NS. (A) Pedigree of the consanguineous family with healthy parents and the son affected by recessive NS harboring the *LZTR1* variant (c.1739T>C/p.L580P) in homozygosity. **(B)** Generation of patient-specific iPSCs by reprogramming of patient's skin fibroblasts via integration-free Sendai virus and genetic correction of the missense variant by CRISPR/Cas9. **(C)** Depiction of the genome editing approach for correction of the missense

variant in *LZTR1* exon 15 by CRISPR/Cas9 and single-stranded oligonucleotide (ssODN) for homology-directed repair. **(D)** Sanger sequencing of the patient-derived iPSCs ($LZTR1^{L580P}$) with the *LZTR1* missense variant in homozygosity and the CRISPR/Cas9-edited heterozygously corrected ($LZTR1^{corr\text{-}het}$) and homozygously corrected ($LZTR1^{corr\text{-}hom}$) iPSCs. **(E)** Molecular karyotyping using a genome-wide microarray demonstrated a high percentage of loss of heterozygosity (LOH) because of consanguinity as well as chromosomal stability of iPSCs after genome editing. **(F)** Patient-specific and CRISPR-corrected iPSCs showed a typical human stem cell-like morphology; scale bar: 100 µm. **(G)** Expression of key pluripotency markers OCT3/4, NANOG, and TRA-1-60 in the generated iPSC lines was assessed by immunocytochemistry; nuclei were counter-stained with Hoechst 33342 (blue); scale bar: 100 µm. **(H)** Flow cytometry analysis of pluripotency marker TRA-1-60 revealed homogeneous populations of pluripotent cells in generated iPSC lines. Gray peaks represent the negative controls.

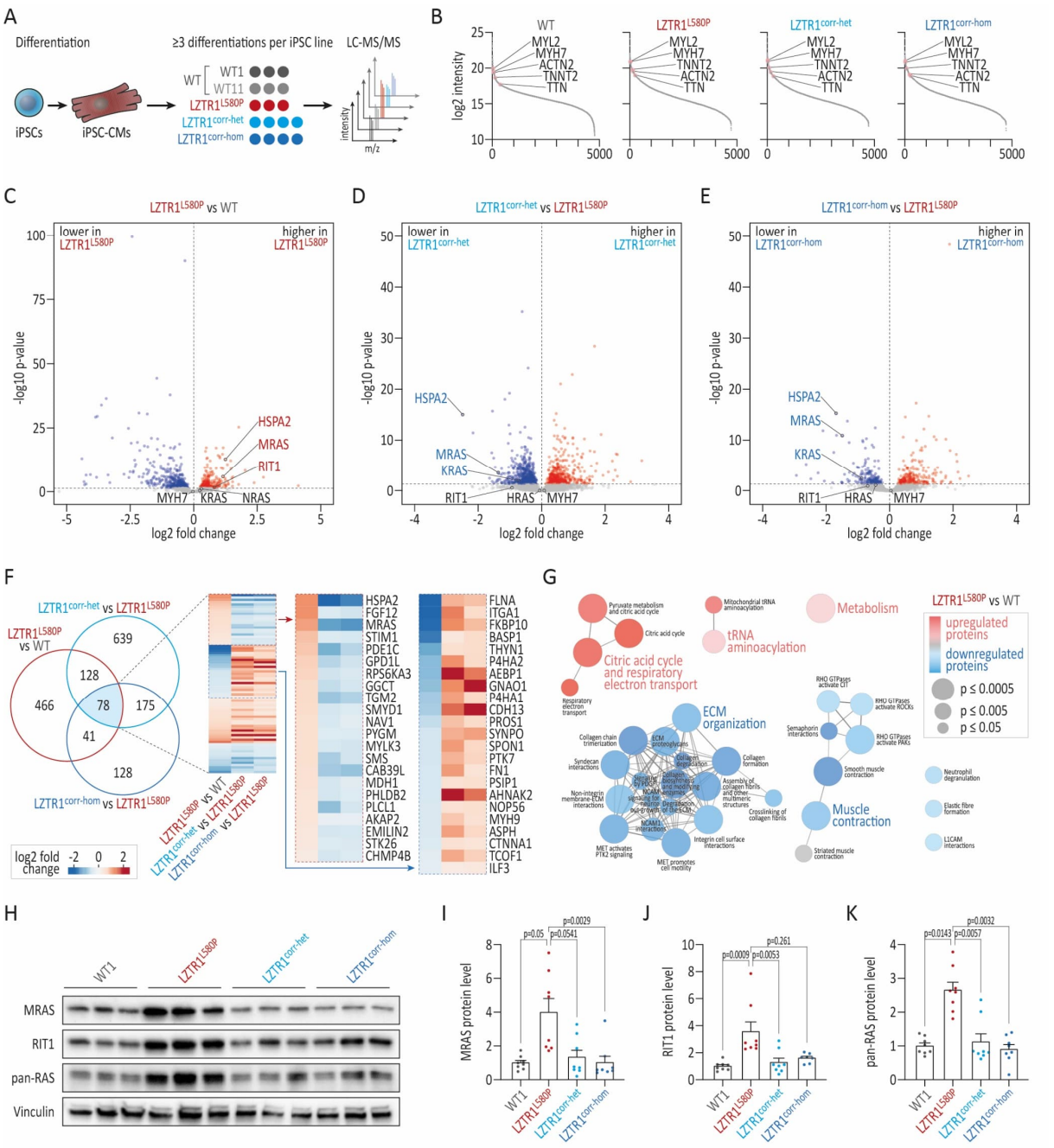

Figure 2: Homozygous *LZTR1^{L580P}* causes accumulation of RAS GTPases. (A) Depiction of the experimental design: two individual WT, the patient-specific, and the two CRISPR-corrected iPSC lines were differentiated into ventricular iPSC-CMs and analyzed by quantitative global proteomics via LC-MS/MS at day 60 of differentiation; n=3-4 individual differentiations per iPSC line. **(B)** Over 4,700 proteins were present in the individual proteomic samples, all showing comparable high abundance of cardiac markers myosin heavy chain β

(*MHY7*), cardiac troponin T (*TNNT2*), α-actinin (*ACTN2*), titin (*TTN*), and ventricular-specific MLC2V (*MYL2*). **(C-E)** Volcano plots representing relative protein abundances comparing patient's versus WT iPSC-CMs (C; LZTR1^{L580P} vs WT), heterozygously corrected versus non-corrected iPSC-CMs (D; LZTR1$^{corr\text{-}het}$ vs LZTR1^{L580P}), and homozygously corrected versus non-corrected iPSC-CMs (E; LZTR1$^{corr\text{-}hom}$ vs LZTR1^{L580P}) revealed high abundance of RAS GTPases in patient samples. **(F)** Comparison of differentially abundant proteins between the three datasets revealed an overlap of 78 proteins, many of which showed opposite abundance in patient's versus CRISPR-corrected iPSC-CMs. **(G)** Reactome pathway enrichment analysis of differentially abundant proteins in LZTR1^{L580P} vs WT displayed dysregulation of cardiac-related pathways and biological processes. **(H)** Representative blots of RAS GTPase levels in WT, patient's, and CRISPR-corrected iPSC-CMs at day 60 of differentiation, assessed by Western blot; Vinculin served as loading control; n=3 individual differentiations per iPSC line. **(I-K)** Quantitative analysis of Western blots for MRAS (I), RIT1 (J), and pan-RAS recognizing HRAS, KRAS, and NRAS (K); data were normalized to total protein and to the corresponding WT samples on each membrane; n=8 independent differentiations per iPSC line. Data were analyzed by nonparametric Kruskal-Wallis test with Dunn correction and are presented as mean ± SEM (I-K).

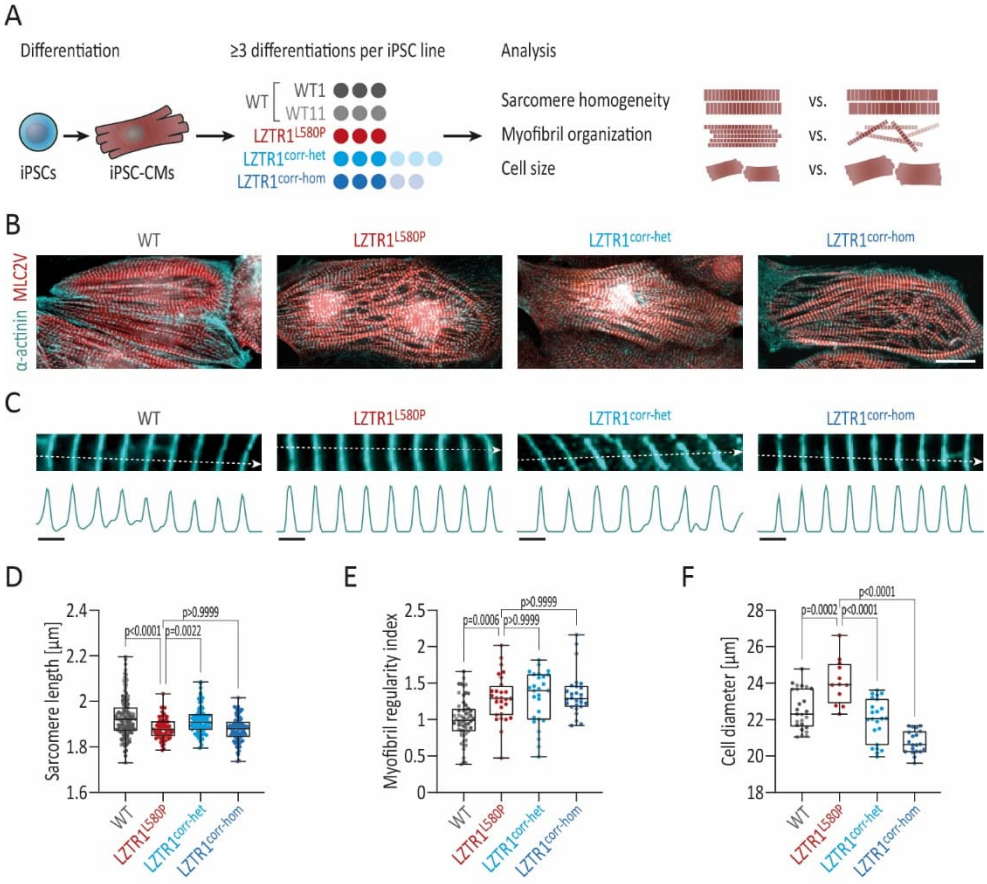

Figure 3: Homozygous *LZTR1^{L580P}* provokes cardiomyocyte hypertrophy. (A) Depiction of the experimental design: two individual WT, the patient-specific, and the two CRISPR-corrected iPSC lines were differentiated into ventricular iPSC-CMs and analyzed for sarcomere length, myofibril organization, and cell size at day 60 of differentiation. **(B)** Representative images of iPSC-CMs stained for α-actinin and ventricular-specific MLC2V indicated a regular and well-organized sarcomeric assembly across all iPSC lines; scale bar: 20 µm. **(C)** Analysis of the mean sarcomere length per cell was based on measurement of multiple α-actinin-stained individual myofibrils; representative myofibrils and corresponding intensity plots are shown; scale bar: 2 µm. **(D)** Quantitative analysis displayed a typical sarcomere length in iPSC-CMs ranging from 1.7 to 2.2 µm across all iPSC lines; n=75-135 cells from 3 individual differentiations per iPSC line. **(E)** Quantitative analysis of the myofibril organization in α-actinin-stained iPSC-CMs, assessed by Fast Fourier Transform algorithm, demonstrated a high

myofibril regularity across all iPSC lines; data were normalized to WT; n=27-58 images from 3 individual differentiations per iPSC line. **(F)** Quantitative analysis of the cell diameter in suspension in singularized iPSC-CMs, assessed by CASY cell counter, revealed a hypertrophic cell diameter in patient's cells, compared with WT and CRISPR-corrected iPSC-CMs; n=12-25 samples from 3-6 individual differentiations per iPSC line. Data were analyzed by nonparametric Kruskal-Wallis test with Dunn correction and are presented as mean ± SEM (D-F).

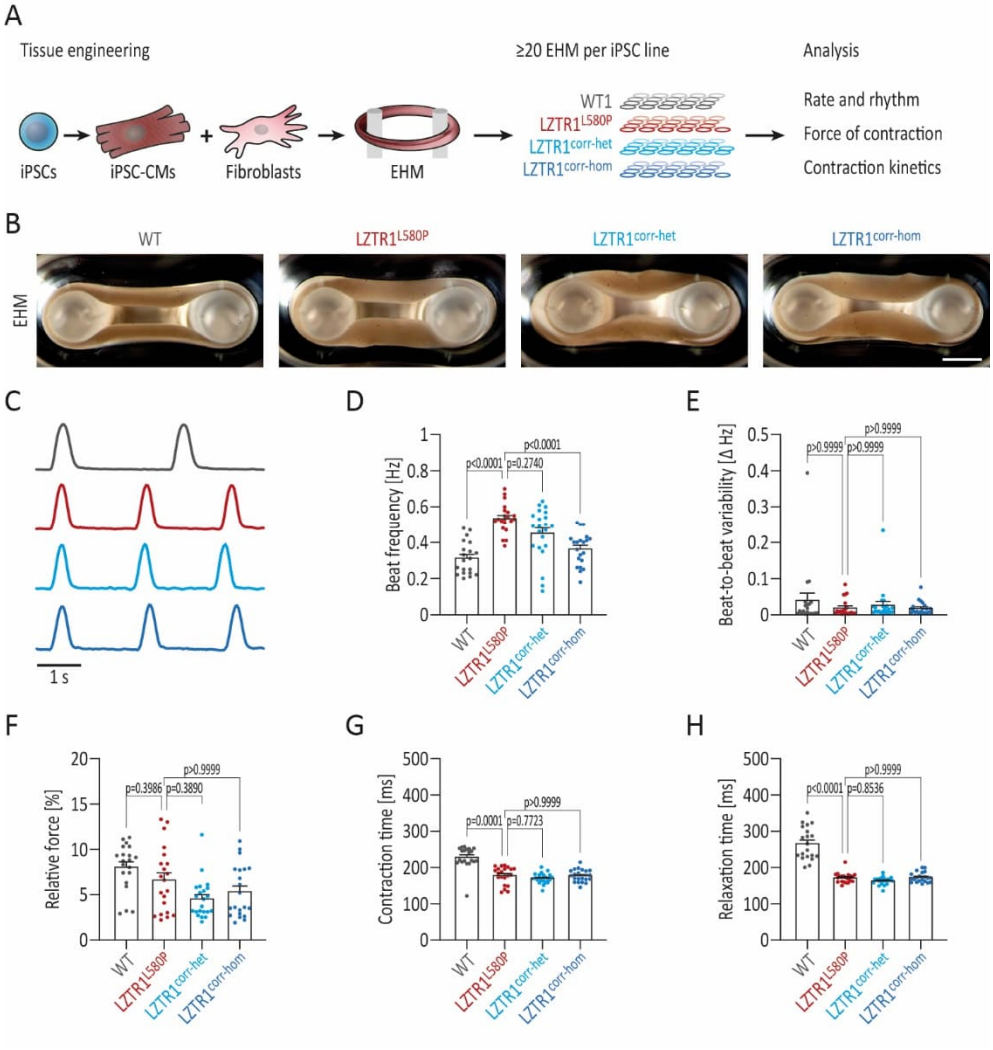

Figure 4: Homozygous *LZTR1^{L580P}* does not compromise contractile function. (A) Depiction of the experimental design: the WT, the patient-specific, and the two CRISPR-corrected iPSC lines were differentiated into ventricular iPSC-CMs and casted at day 30 of differentiation together with fibroblasts in a collagen matrix for generation of EHMs. Tissues were analyzed for rhythmogenicity and contractile parameters by optical recordings at 5-6 weeks post-casting; n=20-22 EHMs from 3 individual differentiations per iPSC line. **(B)** Representative microscopic images of generated EHMs 6 weeks post-casting showing comparable tissue morphologies; scale bar: 1 mm. **(C)** Exemplary contraction traces from optical recordings of EHMs 6 weeks post-casting; peak amplitudes were normalized. **(D)** Quantitative analysis of the beating frequency of spontaneously contracting EHMs displayed

minor differences in patient-derived tissues. **(E)** Quantitative measurement of the beat-to-beat variability of spontaneously contracting EHMs showed equal beating regularities across all tissues. **(F)** Quantitative analysis of the force of contraction, assessed by measuring the relative deflection of flexible poles, identified no significant differences across all iPSC lines. **(G-H)** Quantitative analysis of the contraction kinetics revealed longer contraction times (G) and relaxation times (H) in WT compared to patient's and CRISPR-corrected EHMs. Data were analyzed by nonparametric Kruskal-Wallis test with Dunn correction and are presented as mean ± SEM (D-H).

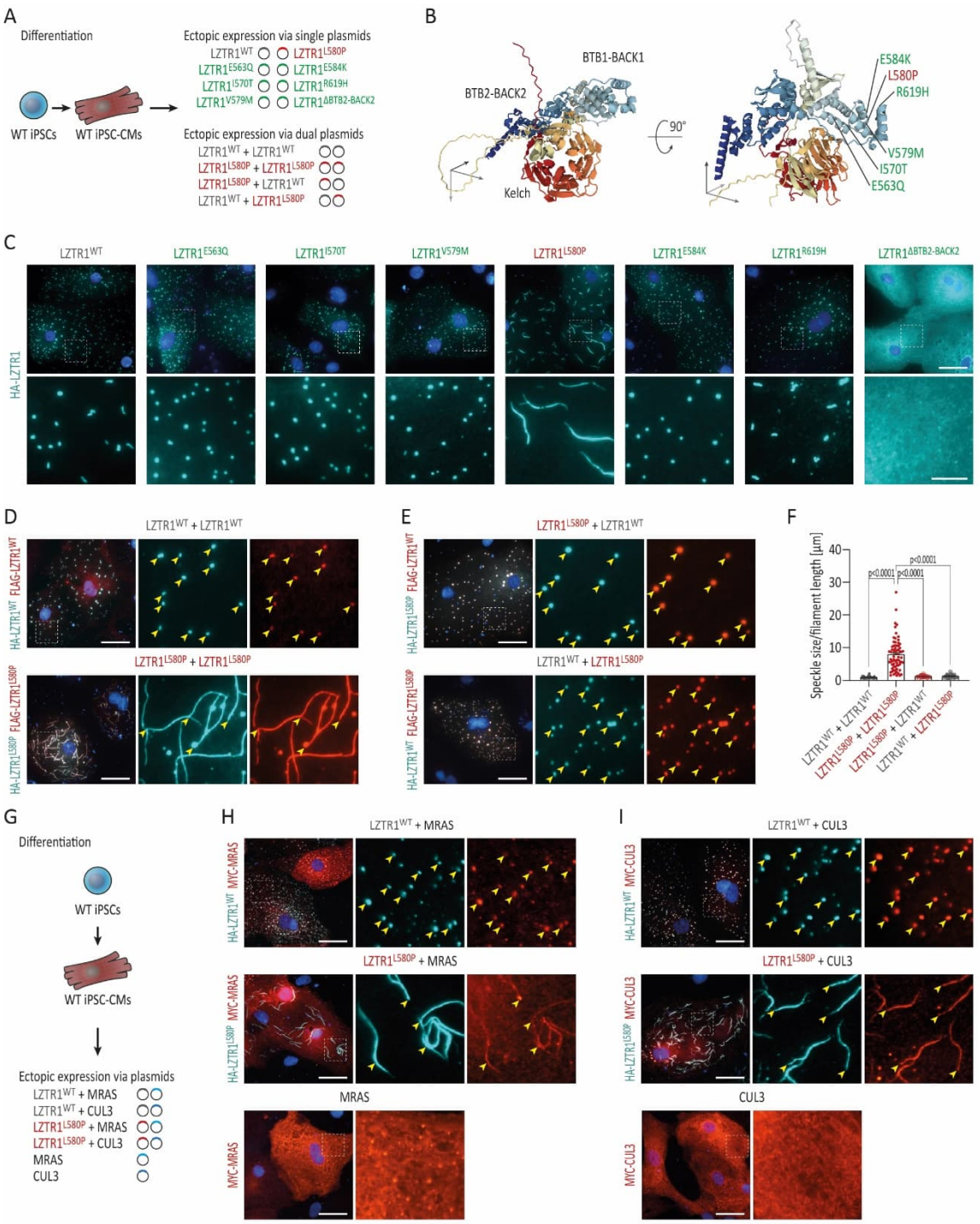

Figure 5: Homozygous *LZTR1^{L580P}* induces polymerization of LZTR1-cullin 3 ubiquitin ligase complexes. (A) Depiction of the experimental design: the WT iPSC line was differentiated into ventricular iPSC-CMs, transfected at day 60 of differentiation with plasmids by lipofection for ectopic expression of LZTR1 variants and analyzed 24 h post-transfection for subcellular localization LZTR1 complexes. **(B)** AlphaFold protein structure of monomeric

LZTR1 highlighting the location of selected variants within the BACK1 domain. **(C)** Representative images of iPSC-CMs after single plasmid transfection stained for HA-tagged LZTR1 revealed that $LZTR1^{WT}$ and most other variants present a speckle-like pattern equally distributed throughout the cytoplasm, whereas missense variant $LZTR1^{L580P}$ forms large filaments; nuclei were counter-stained with Hoechst 33342 (blue); scale bars: 20 µm in upper panel, 5 µm in lower panel. **(D-E)** Representative images of iPSC-CMs after dual plasmid transfection stained for HA-tagged and FLAG-tagged LZTR1 confirmed the filament formation of $LZTR1^{L580P}$ (D), whereas co-expression of $LZTR1^{WT}$ and $LZTR1^{L580P}$ in different combinations resolved the polymer chains (E); nuclei were counter-stained with Hoechst 33342 (blue); scale bar: 20 µm. **(F)** Quantitative analysis of the mean speckle size and mean filament length per cell of HA-tagged LZTR1 in co-transfected iPSC-CMs, assessed by a customized CellProfiler pipeline, confirmed formation of *LZTR1*^{L580P}-induced filaments; n=34-74 cells per condition. **(G)** Experimental outline for co-localization studies: the WT iPSC line was differentiated into ventricular iPSC-CMs, transfected at day 60 of differentiation with plasmids by lipofection for ectopic expression of LZTR1 variants and MRAS or cullin 3 (CUL3), and analyzed 24 h post-transfection. **(H-I)** Representative images of iPSC-CMs after dual plasmid transfection stained for HA-tagged LZTR1 and MYC-tagged MRAS (H) or MYC-tagged CUL3 (I) indicated recruitment of the interaction partners to speckles in $LZTR1^{WT}$ or polymer chains in $LZTR1^{L580P}$; nuclei were counter-stained with Hoechst 33342 (blue); scale bar: 20 µm. Data were analyzed by nonparametric Kruskal-Wallis test with Dunn correction and are presented as mean ± SEM (F).

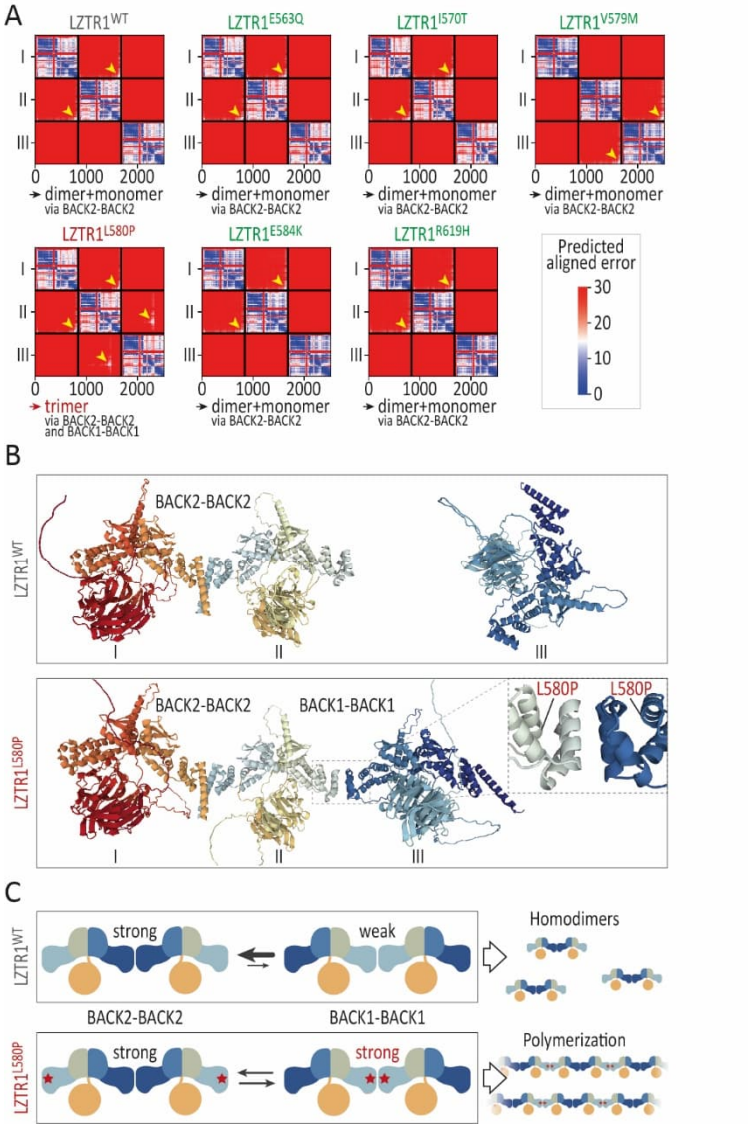

Figure 6: Homozygous *LZTR1^{L580P}* alters binding affinities of dimerization domains. (A) Computational modeling of the top-ranked LZTR1 homo-trimer interactions from selected variants within the BACK1 domain, assessed by the predicted alignment error generated by ColabFold, predicted a dimer plus monomer configuration via BACK2-BACK2 dimerization for LZTR1^{WT} and the other variants, whereas the top-ranked model for LZTR1^{L580P} was predicted to form linear trimers via BACK2-BACK2 and BACK1-BACK1 dimerization; yellow arrows highlight the predicted interaction domains between proteins. **(B)** Visualization of the top-ranked protein interaction models for LZTR1^{WT} assembling as dimer and monomer and for LZTR1^{L580P} forming linear trimers. **(C)** Hypothetical model for LZTR1 complex

formation: whereas LZTR1^{WT} assembles in homo-dimers via the BACK2-BACK2 dimerization domain, LZTR1^{L580P} might alter the binding affinity of the BACK1 domain, causing formation of linear LZTR1 polymer chains via dimerization of both BACK2 and BACK1 domains.

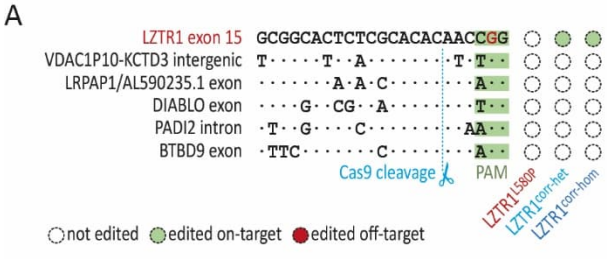

Figure S1: Off-target screening in CRISPR/Cas9-edited iPSCs. (A) Sanger sequencing of the top five predicted off-target regions, ranked by the CFD off-target score using CRISPOR, revealed no off-target editing of CRISPR/Cas9 in CRISPR-corrected iPSCs compared to the patient-derived cells.

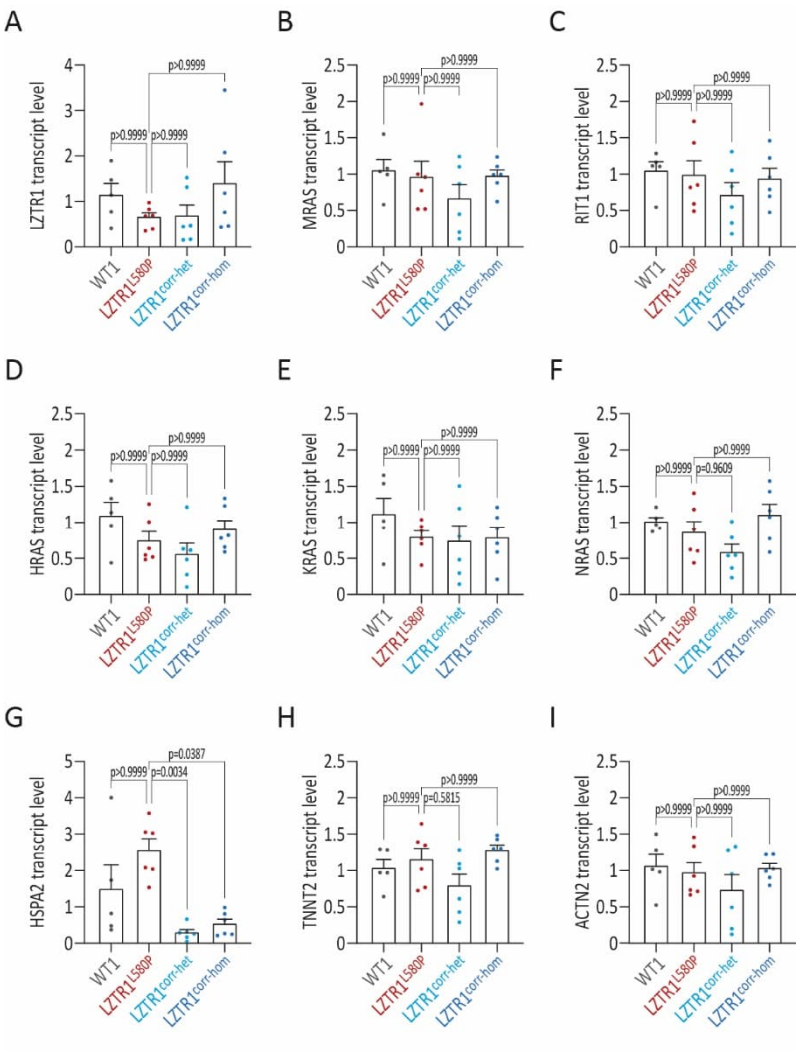

Figure S2: Homozygous *LZTR1^{L580P}* showed no upregulation of RAS GTPases at transcriptional level. (A-I) Quantitative gene expression analysis of *LZTR1* (A), of LZTR1 substrates *MRAS* (B), *RIT1* (C), *HRAS* (D), *KRAS* (E), and *NRAS* (F), of *HSPA2* (G), and of cardiac-specific genes *TNNT2* (H), and *ACTN2* (I) in WT, the patient-specific, and the two CRISPR-corrected iPSC-CMs at day 60 of differentiation, assessed by real-time polymerase chain reaction, revealed no expression differences at transcriptional level across all iPSC lines; samples were analyzed in duplicates and data were normalized to *GAPDH* expression and WT controls; n=5-6 independent differentiations per iPSC line. Data were analyzed by nonparametric Kruskal-Wallis test with Dunn correction and are presented as mean ± SEM (A-I).

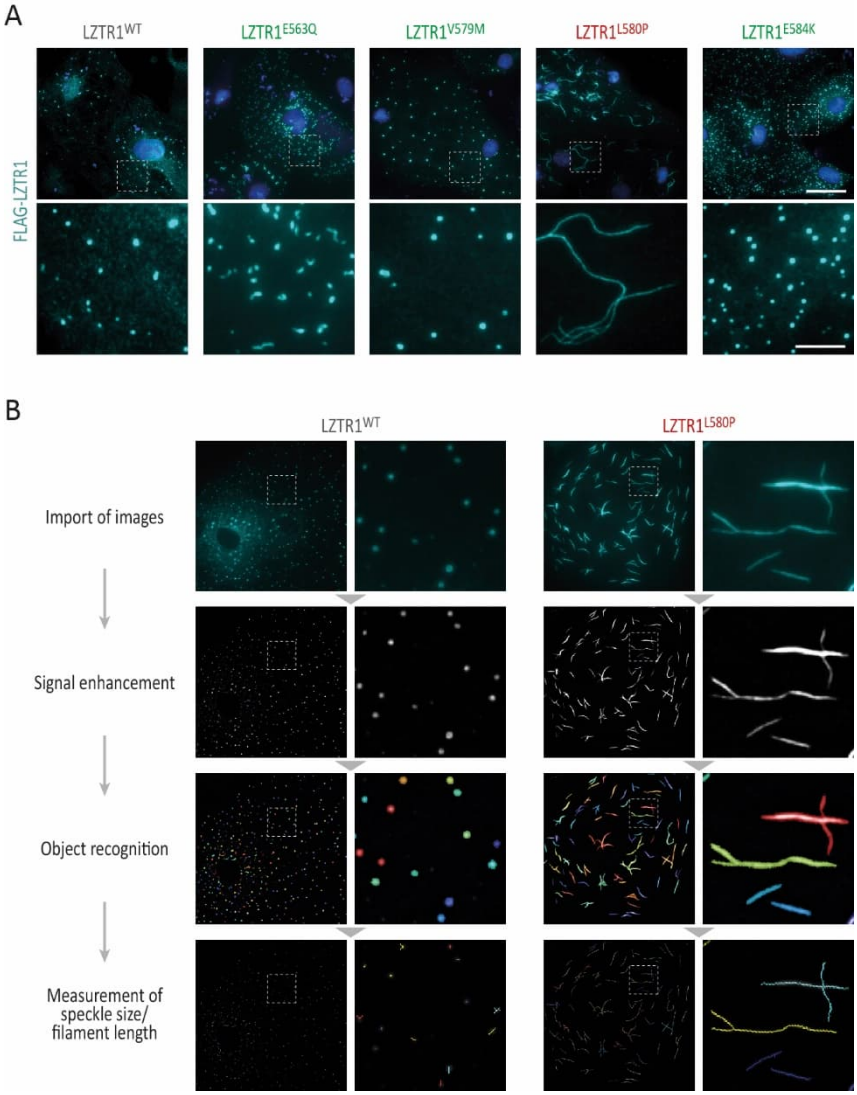

Figure S3: Unique *LZTR1^{L580P}*-induced polymerization of LZTR1 complexes. (A) Representative images of WT iPSC-CMs at day 60 of differentiation after single plasmid transfection stained for FLAG-tagged LZTR1 confirmed that only LZTR1^{L580P} forms large filaments, whereas LZTR1^{WT} and the other variants present a speckle-like pattern; nuclei were counter-stained with Hoechst 33342 (blue); scale bars: 20 µm in upper panel, 5 µm in lower panel. **(B)** Customized CellProfiler pipeline for recognition and quantification of speckle size and filament length in iPSC-CMs with ectopic expression of LZTR1 variants.

A

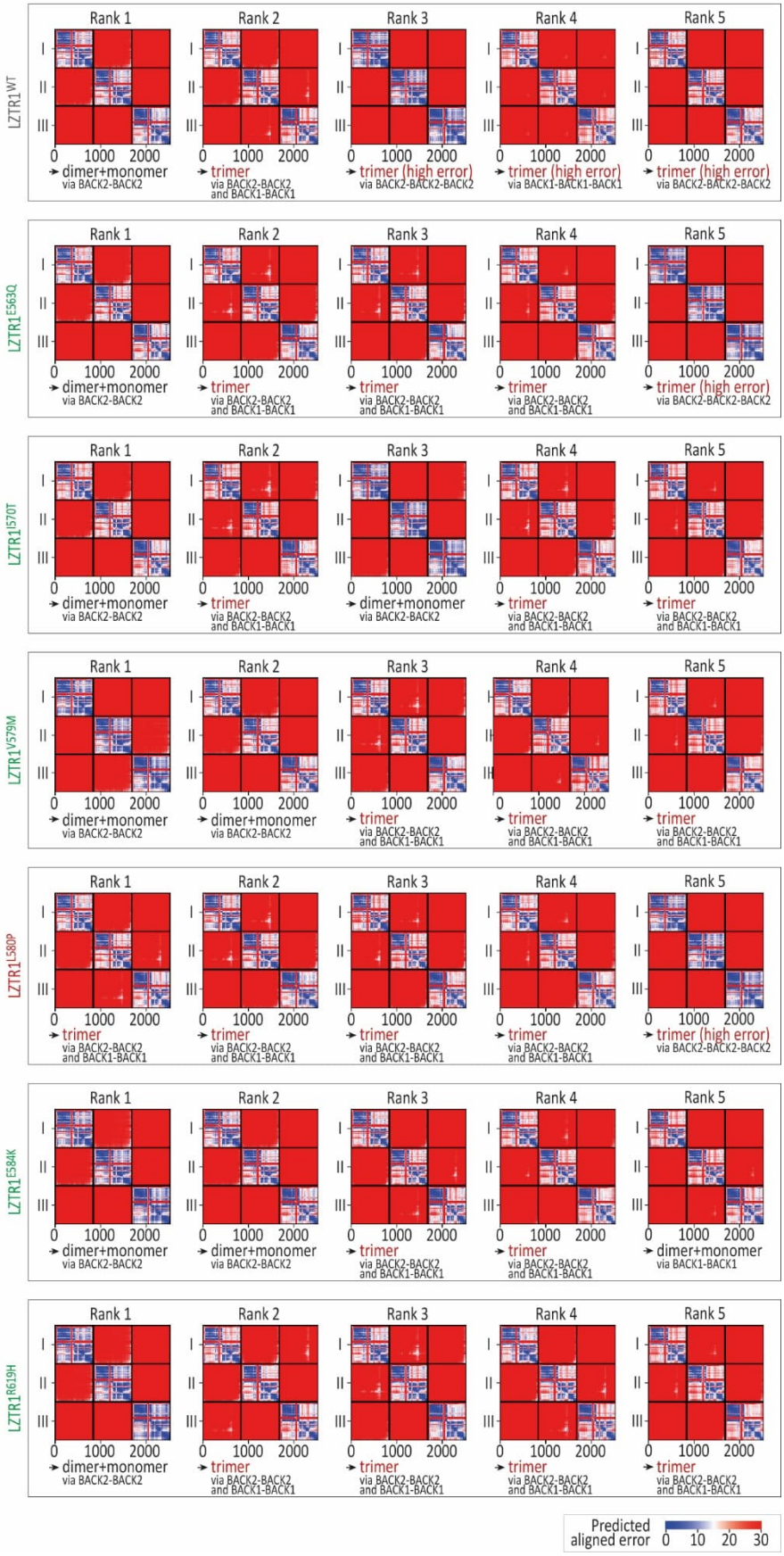
LZTR1 WT
Rank 1
Rank 2
Rank 3
Rank 4
Rank 5
dimer+monomer via BACK2-BACK2
trimer via BACK2-BACK2 and BACK1-BACK1
trimer (high error) via BACK2-BACK2-BACK2
trimer (high error) via BACK1-BACK1-BACK1
trimer (high error) via BACK2-BACK2-BACK2
LZTR1 E563Q
dimer+monomer via BACK2-BACK2
trimer via BACK2-BACK2 and BACK1-BACK1
trimer via BACK2-BACK2 and BACK1-BACK1
trimer via BACK2-BACK2 and BACK1-BACK1
trimer (high error) via BACK2-BACK2-BACK2
LZTR1 I570T
dimer+monomer via BACK2-BACK2
trimer via BACK2-BACK2 and BACK1-BACK1
dimer+monomer via BACK2-BACK2
trimer via BACK2-BACK2 and BACK1-BACK1
trimer via BACK2-BACK2 and BACK1-BACK1
LZTR1 V579M
dimer+monomer via BACK2-BACK2
dimer+monomer via BACK2-BACK2
trimer via BACK2-BACK2 and BACK1-BACK1
trimer via BACK2-BACK2 and BACK1-BACK1
trimer via BACK2-BACK2 and BACK1-BACK1
LZTR1 L580P
trimer via BACK2-BACK2 and BACK1-BACK1
trimer via BACK2-BACK2 and BACK1-BACK1
trimer via BACK2-BACK2 and BACK1-BACK1
trimer via BACK2-BACK2 and BACK1-BACK1
trimer (high error) via BACK2-BACK2-BACK2
LZTR1 E584K
dimer+monomer via BACK2-BACK2
dimer+monomer via BACK2-BACK2
trimer via BACK2-BACK2 and BACK1-BACK1
trimer via BACK2-BACK2 and BACK1-BACK1
dimer+monomer via BACK1-BACK1
LZTR1 R619H
dimer+monomer via BACK2-BACK2
trimer via BACK2-BACK2 and BACK1-BACK1
trimer via BACK2-BACK2 and BACK1-BACK1
trimer via BACK2-BACK2 and BACK1-BACK1
trimer via BACK2-BACK2 and BACK1-BACK1
Predicted aligned error 0 10 20 30

Figure S4: Computational prediction for LZTR1 interactions via ColabFold. (A) The five predicted models for each LZTR1 variant were ranked according to the predicted template modeling score and interactions between the chains were inspected through the predicted alignment error generated by AlphaFold-multimer.

Table S1: Antibodies used for Western blot, immunocytochemistry and flow cytometry.

Primary antibody	**Supplier**	**Resource ID**
α-actinin monoclonal mouse	Sigma-Aldrich	RRID:AB_476766
FLAG monoclonal mouse	Sigma-Aldrich	RRID:AB_262044
HA monoclonal rabbit	Cell Signaling	RRID:AB_1549585
MLC2V polyclonal rabbit	Proteintech	RRID:AB_2147453
MRAS polyclonal rabbit	Proteintech	RRID:AB_10950895
MYC monoclonal mouse	Cell Signaling	RRID:AB_331783
NANOG monoclonal mouse	Thermo Fisher Scientific	RRID:AB_2536677
OCT3/4-PE monoclonal human	Miltenyi Biotec	RRID:AB_2784442
pan-RAS monoclonal mouse	Merck Millipore	RRID:AB_2121151
RIT1 polyclonal rabbit	Abcam	RRID:AB_882379
Tra-1-60 monoclonal mouse	Abcam	RRID:AB_778563
TRA-1-60-Alexa488 monoclonal mouse	BD Biosciences	RRID:AB_1645379
Vinculin monoclonal mouse	Sigma-Aldrich	RRID:AB_477629
Secondary antibody	**Supplier**	**Resource ID**
Alexa488 polyclonal goat anti-rabbit	Thermo Fisher Scientific	RRID:AB_143165
Alexa555 polyclonal donkey anti-mouse	Thermo Fisher Scientific	RRID:AB_2536180
HRP polyclonal donkey anti-rabbit	Sigma-Aldrich	RRID:AB_2722659
HRP polyclonal donkey anti-mouse	Sigma-Aldrich	RRID:AB_772210

Table S2: Primer sequences used for PCR and real-time PCR.

Gene (gDNA)	**Primer**
LZTR1 Ex15	CGAGGCCTTGTTCCTACCTA / GAGGGGCTCACAGTGGTG
Off-target 1	GGTTCAGAAGCACTCATCTCC / AAGCCATCAACCCGAAACAA
Off-target 2	ATGGATCCTGACTGCAACCC / TCTGGGCAGTCTGTGTCTTT
Off-target 3	GATGCCACAATAACCGCTCC / TGAGGAGACGTGGAGAGGAG
Off-target 4	AGTAAGGCGTTTGAGTCCCA / AAGAGGCACATGGATGAGGG
Off-target 5	AACACACTGGGGAAGGAAGT / GAGCTGCTTCCTATCCCCTC
Gene (cDNA)	**Primer**
ACTN2	GCCAGAGAGAAGGATGCAATCAC / AAGCATGGGAACCTGGAATCAA
GAPDH	GGAGCGAGATCCCTCCAAAAT / GGCTGTTGTCATACTTCTCATGG
HRAS	ACGCACTGTGGAATCTCGGCAG / TCACGCACCAACGTGTAGAAGG
HSPA2	GACCAAGGACAATAACCTGCTGG / GGCGTCAATGTCGAAGGTAACC
KRAS	AGTGCCTTGACGATACAG / GCATCATCAACACCCTGTCTT
LZTR1	GAGCCAACTCAAGGAGCACT / CAATGTCCACTGGCTGGTCC
MRAS	CCACCATTGAAGACTCCTACCTG / ACGGAGTAGACGATGAGGAAGC
NRAS	GGCAATCCCATACAACCCTGAG / GAAACCTCAGCCAAGACCAGAC
RIT1	TTCATCAGCCACCGATTCCC / GCAGGCTCATCATCAATACGG
TNNT2	ACAGAGCGGAAAAGTGGGAAG / TCGTTGATCCTGTTTCGGAGA

Table S3: Plasmids used for ectopic expression studies.

Plasmid	**Source**
pcDNA3-HA-LZTR1-WT	modified from addgene plasmid #13512
pcDNA3-FLAG-LZTR1-WT	modified from pcDNA3-HA-LZTR1-WT
pcDNA3-HA-LZTR1-E563Q	modified from pcDNA3-HA-LZTR1-WT
pcDNA3-FLAG-LZTR1-E563Q	modified from pcDNA3-FLAG-LZTR1-WT
pcDNA3-HA-LZTR1-I570T	modified from pcDNA3-HA-LZTR1-WT
pcDNA3-HA-LZTR1-V579M	modified from pcDNA3-HA-LZTR1-WT
pcDNA3-FLAG-LZTR1-V579M	modified from pcDNA3-FLAG-LZTR1-WT
pcDNA3-HA-LZTR1-L580P	modified from pcDNA3-HA-LZTR1-WT
pcDNA3-FLAG-LZTR1- L580P	modified from pcDNA3-FLAG-LZTR1-WT
pcDNA3-HA-LZTR1-E584K	modified from pcDNA3-HA-LZTR1-WT
pcDNA3-FLAG-LZTR1-E584K	modified from pcDNA3-FLAG-LZTR1-WT
pcDNA3-HA-LZTR1-R619H	modified from pcDNA3-HA-LZTR1-WT
pcDNA3-HA-LZTR1-ΔBTB2-BACK2	modified from pcDNA3-HA-LZTR1-WT
pCMV6-MRAS-Myc-DDK	Origene plasmid #RC212259
pcDNA3-Myc-CUL3	Addgene plasmid #19893